

REPORT DOCUMENTATION PAGE			Form Approved OMB No. 0704-0188		
<p>Public reporting burden for this collection of information is estimated to average 1 hour per response, including the time for reviewing instructions, searching existing data sources, gathering and maintaining the data needed, and completing and reviewing this collection of information. Send comments regarding this burden estimate or any other aspect of this collection of information, including suggestions for reducing this burden to Department of Defense, Washington Headquarters Services, Directorate for Information Operations and Reports (0704-0188), 1215 Jefferson Davis Highway, Suite 1204, Arlington, VA 22202-4302. Respondents should be aware that notwithstanding any other provision of law, no person shall be subject to any penalty for failing to comply with a collection of information if it does not display a currently valid OMB control number. PLEASE DO NOT RETURN YOUR FORM TO THE ABOVE ADDRESS.</p>					
1. REPORT DATE (DD-MM-YYYY) May 2008		2. REPORT TYPE Thesis		3. DATES COVERED (From - To) 1 May 2008 – 02 March 2015	
4. TITLE AND SUBTITLE COMPARISON BETWEEN PREDICTIONS AND EXPERIMENTAL MEASUREMENTS FOR AN EIGHT POCKET ANNULAR HYDROSTATIC THRUST BEARING			5a. CONTRACT NUMBER FA9300-04-C-0016		
			5b. GRANT NUMBER		
			5c. PROGRAM ELEMENT NUMBER		
6. AUTHOR(S) MICHAEL FORSBERG			5d. PROJECT NUMBER		
			5e. TASK NUMBER		
			5f. WORK UNIT NUMBER Q0BY		
7. PERFORMING ORGANIZATION NAME(S) AND ADDRESS(ES) Air Force Research Laboratory (AFMC) AFRL/RQRC 10 E. Saturn Blvd Edwards AFB, CA 93524-7680			8. PERFORMING ORGANIZATION REPORT NO.		
9. SPONSORING / MONITORING AGENCY NAME(S) AND ADDRESS(ES) Air Force Research Laboratory (AFMC) AFRL/RQR 5 Pollux Drive Edwards AFB, CA 93524-7048			10. SPONSOR/MONITOR'S ACRONYM(S)		
			11. SPONSOR/MONITOR'S REPORT NUMBER(S) AFRL-RQ-ED-OT-2015-037		
12. DISTRIBUTION / AVAILABILITY STATEMENT Approved for public release; distribution unlimited					
13. SUPPLEMENTARY NOTES PA Case Number: #15072; Clearance Date: 2/10/2015 This is a Master's Thesis based upon work subcontracted to Texas A&M University by Northrop Grumman under the USET contract. The work was completed in 2008 and the advisor is looking to have the thesis made publicly releasable.					
14. ABSTRACT A test rig was designed, produced, and used to test a hydrostatic thrust bearing geometry. In a non-rotational configuration, this test rig uses a hydraulic shaker to load the thrust bearing and rotor. The test hydrostatic thrust bearing has an outer radius of 38.1 mm and an inner radius of 20.32 mm. The bearing has eight pockets spaced evenly at the mid-radius with a supply orifice located in the center of each pocket. This applied force is then reacted by a stationary pedestal that a thrust bearing rests against. The hydrostatic thrust bearing was tested at 3.45, 10.34, and 17.24 bar supply pressure with water at approximately 38oC; each thrust bearing supply pressure was tested with at least ten applied loads spanning the loading range predicted by XLHydroTHRUST®. The test results are compared to predictions for flow rate and load versus bearing clearances from XLHydroTHRUST®. Predictions correlated reasonably well for flow and load especially for test clearances higher than 0.076 mm where the predictions and measurements agree within 20%. The differences between predictions and measurements may be due to the observed discharge coefficient and thrust bearing face misalignment at low clearance. This discharge coefficient must be given a constant value for XLHydroTHRUST®, but significant changes were observed when extracted from the test data. Further investigation may be warranted to account for this discrepancy.					
15. SUBJECT TERMS N/A					
16. SECURITY CLASSIFICATION OF:			17. LIMITATION OF ABSTRACT SAR	18. NUMBER OF PAGES 58	19a. NAME OF RESPONSIBLE PERSON G. Ruderman
a. REPORT Unclassified	b. ABSTRACT Unclassified	c. THIS PAGE Unclassified		19b. TELEPHONE NO (include area code) N/A	

COMPARISON BETWEEN PREDICTIONS AND EXPERIMENTAL
MEASUREMENTS FOR AN EIGHT POCKET ANNULAR HYDROSTATIC
THRUST BEARING

A Project Report

By

MICHAEL FORSBERG

Submitted

In partial fulfillment of the requirements for the degree of

MASTER OF SCIENCE

May 2008

Major Subject: Mechanical Engineering

Abstract

Comparison Between Predictions and Experimental Measurements for an Eight Pocket Annular Hydrostatic Thrust Bearing

(May 2008)

Michael Forsberg, B.S.M.E., Oklahoma State University

Chair of Advisory Committee: Dr. Dara Childs

A test rig was designed, produced, and used to test a hydrostatic thrust bearing geometry. In a non-rotational configuration, this test rig uses a hydraulic shaker to load the thrust bearing and rotor. The test hydrostatic thrust bearing has an outer radius of 38.1 mm and an inner radius of 20.32 mm. The bearing has eight pockets spaced evenly at the mid-radius with a supply orifice located in the center of each pocket. This applied force is then reacted by a stationary pedestal that a thrust bearing rests against. The hydrostatic thrust bearing was tested at 3.45, 10.34, and 17.24 bar supply pressure with water at approximately 38°C; each thrust bearing supply pressure was tested with at least ten applied loads spanning the loading range predicted by XLHydroTHRUST®.

The test results are compared to predictions for flow rate and load versus bearing clearances from XLHydroTHRUST®. Predictions correlated reasonably well for flow and load especially for test clearances higher than 0.076 mm where the predictions and measurements agree within 20%.

The differences between predictions and measurements may be due to the observed discharge coefficient and thrust bearing face misalignment at low clearance. This discharge coefficient must be given a constant value for XLHydroTHRUST®, but significant changes were observed when extracted from the test data. Further investigation may be warranted to account for this discrepancy.

Acknowledgements

I would like to thank Dr. Childs and Dr. San Andrés for giving me this opportunity to work on this project and finish my part in it. I would also like to express my appreciation for my coworkers at the Turbomachinery Laboratory, especially Adolpho Delgado, who I imposed on regularly for help. I would finally like to thank Carlos Valles who designed the test rig with me as well as Fernando Ramirez and Scott Wilson for working with me during set up and testing, and for always asking questions.

Table of Contents

Abstract	ii
Acknowledgements	iii
Table of Contents	iv
List of Figures	v
List of Tables	vii
Previous Test Rigs	1
Previous Thrust Bearing Research	4
Test Rig Description	6
Instrumentation.....	10
Non-Rotating Test	
Procedure	15
Non-Rotating Test	
Results	17
Conclusions	32
References	33
 Appendix A –	
Flow loop schematic with pertinent instrumentation included.....	35
 Appendix B –	
Table of instrumentation and accessories used.....	37
 Appendix C –	
Test thrust bearing rotor thrust disk plane equation derivation.....	39
 Appendix D –	
Detailed figures of misalignment across bearing face and pocket pressures.....	43
 Appendix E –	
Uncertainty analysis of experimental measurements.....	47

List of Figures

Figure 1: Orion high speed test rig used by New [1].....	1
Figure 2: Harada test rig for hydrostatic thrust bearing testing [5].....	2
Figure 3: Gardner back-to-back test rig for testing hydrodynamic bearings [7].....	3
Figure 4: Test rig used for testing of double hydrodynamic thrust bearings [9].....	4
Figure 5: Scaled load versus scaled film thickness and flow rate for the hydrostatic thrust bearing tested in [6].....	5
Figure 6: Schematic of hydrostatic thrust bearing test rig rotating configuration.....	6
Figure 7: Test thrust bearing and test thrust bearing air seal flow paths.....	7
Figure 8: Schematic of hydrostatic thrust bearing test rig non-rotating testing configuration.....	8
Figure 9: Static configuration load path.....	9
Figure 10: Front view of test thrust bearing.....	9
Figure 11: Locations of eddy current proximity probes during non-rotating test.....	10
Figure 12: Example calibration curve for a eddy current proximity probe used on the hydrostatic thrust bearing test rig.....	12
Figure 13: Locations of the inner and outer radius thermocouples on the test thrust bearing.....	12
Figure 14: Inlet pressure sensors for journal bearings and test thrust bearing.....	13
Figure 15: Location of pressure taps for pressure measurement.....	14
Figure 16: Tilt adjustment shims for the correction of test thrust bearing tilt in static testing configuration.....	15
Figure 17: Orifice loss coefficient calculated from test data for 3.45, 10.34, and 17.24 bar test thrust bearing supply pressure tests.....	18
Figure 18: Orifice Reynolds number calculated from test data for 3.45, 10.34, and 17.24 bar test thrust bearing supply pressure tests.....	19
Figure 19: Outer radius Reynolds number calculated from test data for 3.45, 10.34, and 17.24 bar test thrust bearing supply pressure tests.....	20
Figure 20: Misalignment over the bearing face about the x and y axis for 3.45, 10.34, and 17.24 bar test thrust bearing supply pressure test. Lines mark desired limits for misalignment ± 0	21
Figure 21: Measured inlet flow rates and flow out through inner radius of thrust bearing for 3.45, 10.34, and 17.24 bar thrust bearing supply pressures with uncertainty bars shown.....	22
Figure 22: Measured and predicted inlet flow rates for 3.45, 10.34, and 17.24 bar supply pressures.....	23
Figure 23: Measured exhaust flow rate through the inner thrust bearing radius and predictions from XLHydroTHRUST®. Flow rates plotted for 3.45, 10.34, and 17.24 bar.....	24
Figure 24: Pocket pressure ratios over the tested clearance range for 3.45, 10.34, and 17.24 bar thrust bearing supply pressure.....	25
Figure 25: Experimentally measured test thrust bearing clearance versus load and XLHydroTHRUST® predictions.....	26

Figure 26: Clearance versus load measurements with fourth order polynomial curve fit for 3.45 bar test thrust bearing supply pressure.....	28
Figure 27: Estimated clearance versus axial inverse flexibility for 3.45 bar test thrust bearing supply pressure.....	29
Figure 28: Clearance versus load measurements with two fourth order polynomial curve fit for 10.34 bar test thrust bearing supply pressure.....	29
Figure 29: Estimated clearance versus axial inverse flexibility for 10.34 bar test thrust bearing supply pressure.....	30
Figure 30: Clearance versus load measurements with two fourth order polynomial curve fit for 17.24 bar test thrust bearing supply pressure.....	31
Figure 31: Estimated clearance versus axial inverse flexibility for 17.24 bar test thrust bearing supply pressure.....	31
Figure 32: Hybrid thrust bearing test rig flow loop with select instrumentation locations included.....	36
Figure 33: Layout geometry of eddy current sensors on test thrust bearing support.....	40
Figure 34: Depiction of the three points measured with the proximity probes on the test thrust bearing thrust disk face.....	41
Figure 35: Misalignment over the bearing face about the x and y axis for 3.45 bar test thrust bearing supply pressure.....	44
Figure 36: Misalignment over the bearing face about the x and y axis for 10.34 bar test thrust bearing supply pressure.....	44
Figure 37: Misalignment over the bearing face about the x and y axis for 17.24 bar test thrust bearing supply pressure.....	45
Figure 38: Pocket pressure ratios over the tested clearance range for 3.45 bar thrust bearing supply pressure.....	45
Figure 39: Pocket pressure ratios over the tested clearance range for 10.34 bar thrust bearing supply pressure.....	46
Figure 40: Pocket pressure ratios over the tested clearance range for 17.24 bar thrust bearing supply pressure.....	46

List of Tables

Table 1: Important dimensions and parameters for the tested thrust bearing.....	10
Table 2: Table of DAQ board specifications [15].....	14
Table 3: Average orifice discharge coefficients used for XLHydroTHRUST® predictions.....	20
Table 4: Vertical and horizontal positions of proximity probes on thrust bearing support from bearing center.....	40
Table 5: Coordinates of the three proximity probe points	41

Nomenclature

A_0 = Area of the thrust bearing inlet orifice (m^2)

C_d = Orifice discharge coefficient

D_{Orifice} = Diameter of orifice (m)

E_N = Uncertainty associated with term "N"

f_{mn} = Flexibility coefficient for direction "m" from variable "n"

F_z = Load on bearing face

M_1 = Misalignment in the x direction (mm/mm)

M_2 = Misalignment in the y direction (mm/mm)

M_a = Moment acting in "a"

$P_{\text{Atmospheric}}$ = Atmospheric pressure

P_{Exhaust} = Pressure bearing exhausts into

P_{Pocket} = Pocket pressure

P_{Ratio} = Pressure ratio

P_R = Recess (pocket) pressure (Pa)

P_{Supply} = Supply pressure

P_S = Supply pressure (Pa)

$\text{Re}_{\text{Orifice}}$ = Orifice Reynolds number

$\text{Re}_{\text{OuterRadius}}$ = Outer radius Reynolds number

V_{Orifice} = Fluid velocity through orifice (m/s)

$V_{\text{OuterRadius}}$ = Fluid velocity through thrust bearing outer radius (m/s)

Z_a = Gap reading from proximity probe "a"

Z = Center clearance of thrust bearing (m)

μ = Dynamic viscosity ($\text{N} \cdot \text{s}/\text{m}^2$)

ρ = Working fluid density (kg/m^3)

Φ_c = Misalignment angle about axis "c"

Previous Test Rigs

Numerous test rigs have been designed for experimentation with thrust bearings. These test rigs fall into two categories: single thrust bearing test rigs where the load is applied by pushing the rotor to apply loading to a stationary thrust bearing; and multiple-thrust-bearing test rigs with the load applied through a thrust bearing and transmitted to a separate thrust bearing where the load is reacted. For tests involving shaft rotation, multiple-thrust-bearing rigs are preferred.

New [1] describes a multiple-thrust-bearing test rig for testing hydrodynamic thrust bearings seen in Figure 1.

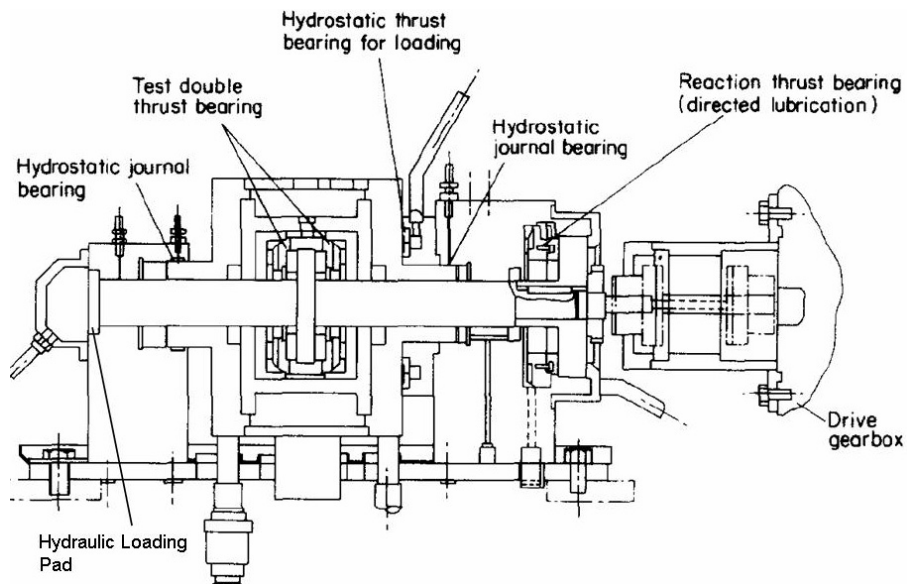


Figure 1: Orion high speed test rig used by New [1]

In this test rig the load is applied to the housing containing the test thrust bearing with a hydrostatic thrust bearing. The test thrust bearing then transmits the load through the rotor, which is supported on a pair of hydrostatic journal bearings, where it is reacted with a hydraulic loading pad. The load is then measured with the hydraulic loading system. To measure the torque exerted on the thrust bearings, as well as to allow free axial movement for loading, the housing containing the thrust bearings is mounted on hydrostatic bearings. This design allows the housing to rotate freely, which loads a spring balance and measures the torque. Additionally, the test bearings are instrumented

to measure the clearance and temperatures while flow rates are measured outside of the test rig. Gregory [2], Neal [3], and Horner et al [4] describe similar test rigs.

Harada et al [5] uses the multiple thrust bearing test rig in Figure 2.

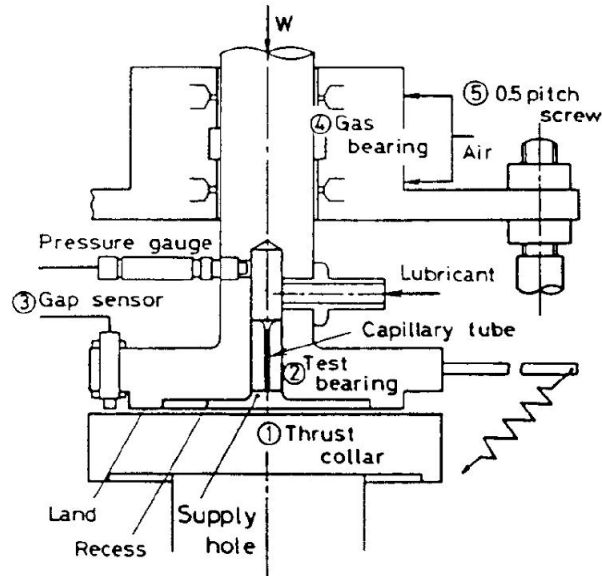


Figure 2: Harada test rig for hydrostatic thrust bearing testing [5]

The Harada test rig uses a piston floated on gas bearings to support and load the test thrust bearing. This load is then transmitted through the rotor to a set of ball bearings which react it. The thrust bearing clearance is measured by three eddy current proximity probes located 120° from each other, which allows for more detailed information about the clearance profile. Finally, temperature is measured at the inlet and outlet, and flow rate is measured into the bearing.

Wang and Yamaguchi [6] also use a test rig of a similar layout. Their test rig though is vertically aligned and uses a different loading and support mechanism for the test thrust bearing. On the Wang test rig, an oil cylinder loads a mechanism through which a hydrostatic bearing transfers the load to the test thrust bearing. The load is then transmitted as in the Harada test rig. The load-transferring hydrostatic thrust bearing allows the measurement of the torque through a load cell.

Gardner [7] describes a different type of multiple-thrust-bearing test rig. This test rig places two thrust bearings between the thrust disks of the rotor as seen in Figure 3.

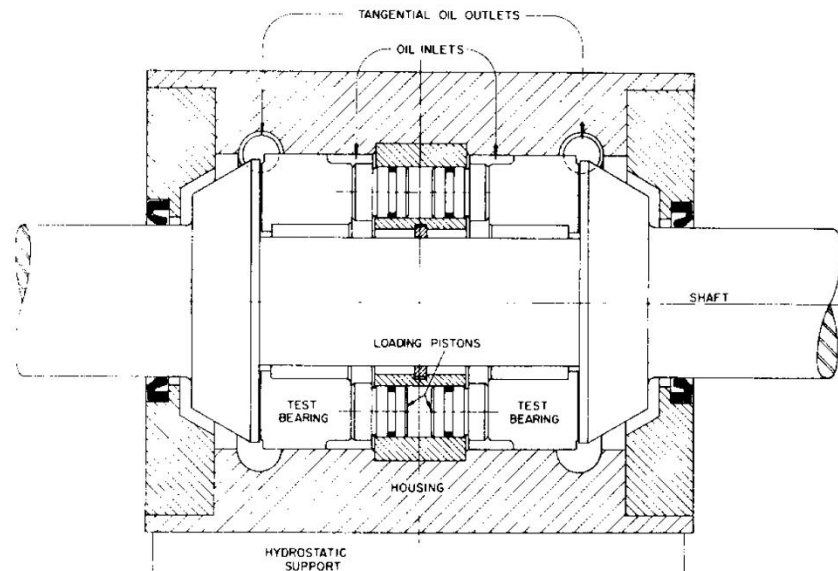


Figure 3: Gardner back-to-back test rig for testing hydrodynamic bearings [7]

This thrust-bearing test-rig style is referred to as a back-to-back configuration. The back-to-back arrangement allows for the use of hydraulic loading pistons between the thrust bearings. The pistons load the test bearing; the load is then reacted with the other bearing after the rotor transmits the load. The load is measured from the supply pressure to the hydraulic loading pistons. The thrust bearing assembly is also supported on a hydrostatic support system, which allows the torque on the thrust bearings to be measured with a load cell. Temperature on the bearing pad, inlet pressures, and flow rates are also measured with this test rig.

Glavatskih [8] presents a very similar back-to-back thrust bearing test rig, and Glavatskih [9] describes the test rig for testing double thrust bearings in Figure 4.

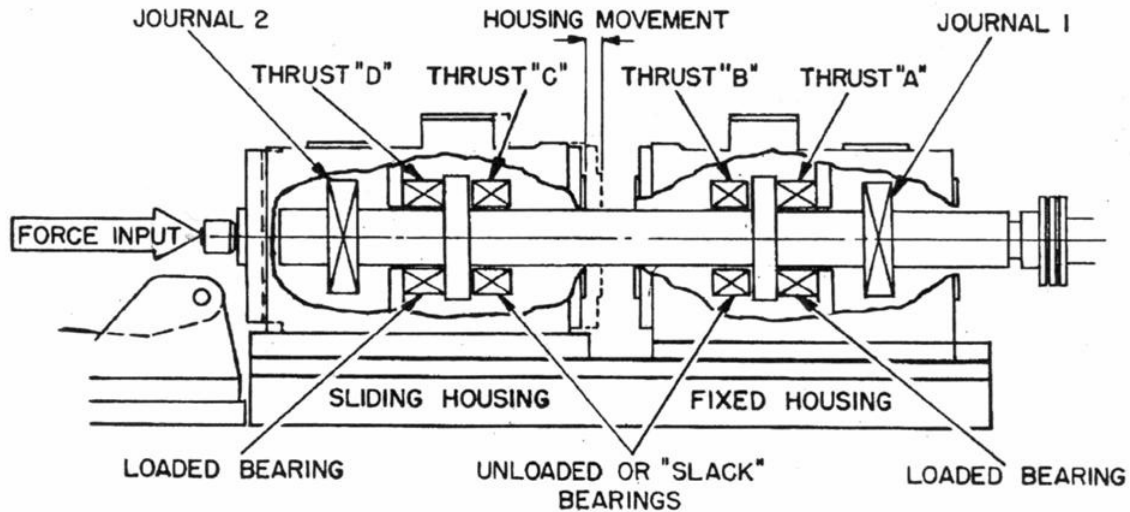


Figure 4: Test rig used for testing of double hydrodynamic thrust bearings [9]

The test rig in Figure 4 is composed of two similar sections each housing a thrust bearing set and a journal bearing. One section is allowed to move freely in the axial direction to apply load to the rotor. The other section is secured and reacts the applied force from the sliding section.

Previous Thrust Bearing Research

Thrust bearings are a critical part of any rotating machine to maintain correct axial positioning and counteract axial loads. As such, knowledge of thrust bearing static and dynamic characteristics is crucial for predicting a turbomachine's position under operating conditions. This review examines the currently available experimental information in the literature on hydrodynamic and hydrostatic bearings.

Hydrostatic bearings rely on external pressurization to support a load. The bearing fluid is supplied into a pocket or the lands through an orifice or capillary feed. The fluid then flows to the sides through the lands and exits to a lower ambient pressure. The resulting high pressure over the bearing surface provides the necessary force to react the applied load. The performance of this type of bearing depends upon the size of the lands, pockets, fluid properties, fluid inlets, clearance, and most importantly the supply pressure. If a hydrostatic bearing experiences rotation it is referred to as a hybrid bearing, and the influence of the rotation must be taken into account as the rotation can have a significant effect on the bearing performance. Hybrid bearings may also

incorporate tilting pads that can significantly alter the behavior of the thrust bearing. Rowe [11] offers additional general information on hydrostatic and hybrid bearings.

San Andrés [12] presents a model for predicting hybrid thrust bearing performance that includes fluid inertia, flow turbulence, and fluid compressibility. This model uses the bulk-flow model that relates shear at the surfaces of the bearing to the average fluid-flow velocities relative to the walls. Separate equations are presented for the lands and recesses (pockets) with the conditions calculated at the edge of the pockets providing boundary conditions for the lands equation. A first-order perturbation is implemented to calculate the bearing force coefficients. The zeroth order equations are solved using a controlvolume scheme. Numerical results are then provided for a hybrid bearing system. Discussions on this model are expanded in San Andrés [13] where effects of collar misalignment are discussed and predicted to noticeably affect flow rate, stiffness, and damping.

Wang and Yamaguchi [6] present flow rate and clearance results from testing a center pocket hydrostatic thrust bearing with oil. This bearing has a pocket in the center of the thrust bearing and has no inner radius discharge as opposed the bearing tested here with a ring of fluid-supplied pockets with an inner discharge. Figure 5 shows their relevant results.

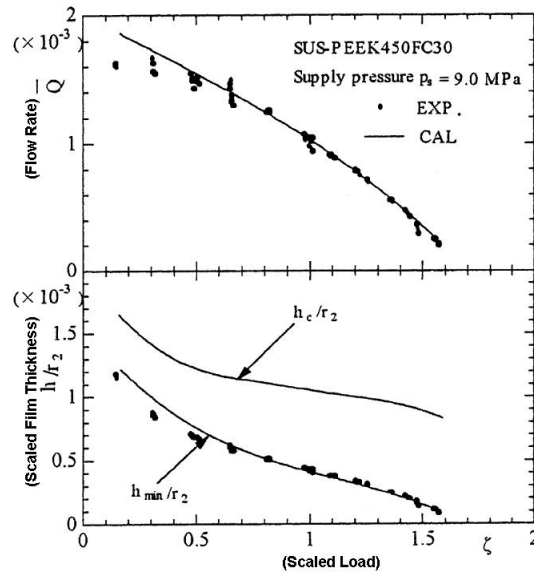


Figure 5: Scaled load versus scaled film thickness and flow rate for the hydrostatic thrust bearing tested in [6].

Measured flow rates in [6] show a decreasing second-order trend with increasing scaled load indicating that resistance to flow increases with the decreasing clearance caused by the load. Clearance shows a higher-order trend, decreasing with increasing scaled load. Similar results are also presented for this geometry in Harada et al [5].

Test Rig Description

This section presents the hydrostatic thrust bearing test rig. The two configurations planned and used to date are described, as well as the intended goals of each configuration.

Figure 6 shows a cross section of the hydrostatic test thrust bearing rig in its rotating configuration.

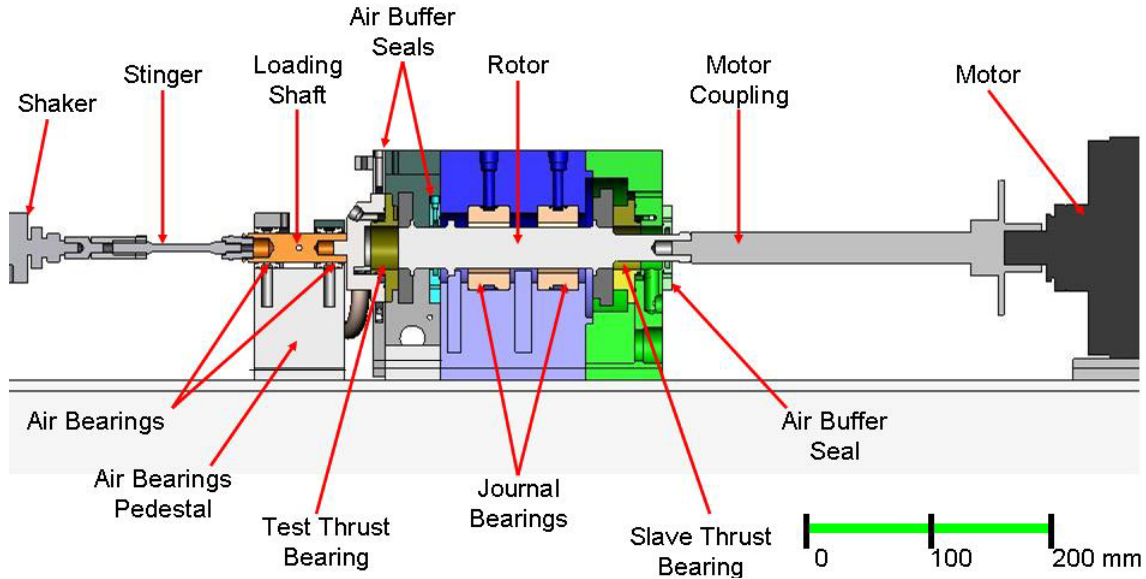


Figure 6: Schematic of hydrostatic thrust bearing test rig rotating configuration

Figure 6 shows the face-to-face thrust-bearing configuration mounted on a rotor that is supported by two hydrostatic journal bearings. This configuration is similar to the back-to-back configuration used by Gardner [7] and Glavatskih [8] but with the thrust bearings facing the outside of the rotor thrust disks. This allows the test bearing to be a single piece instead of split and allows for a lighter loading mechanism. The load is applied to the system with a hydraulic shaker that moves the test thrust bearing axially thus applying load to the rotor. This load is then transmitted by the rotor to the slave thrust bearing where it is reacted.

The test rig uses two bearing-supported shafts. The first is the nonrotating loading shaft supported on two air bearings. These bearings are supplied with filtered 10.34 bar shop air and allow the loading shaft to move axially with very little friction with changing load.

The test rotor is supported by two flexible-pivot tilting-pad hydrostatic journal bearings. The journal bearings are supplied with water from the same source as the test bearings and allow the rotor to move axially with varied loading as well as rotate. An electric motor attaches to the slave bearing side of the rotor through a flexible coupling and drives the rotor.

The test thrust bearing section of the test rig is isolated from the other bearings by an air buffer seal to enable measurement of the test thrust bearing exhaust flow without contamination from the other bearings' exhaust flow as shown in Figure 7.

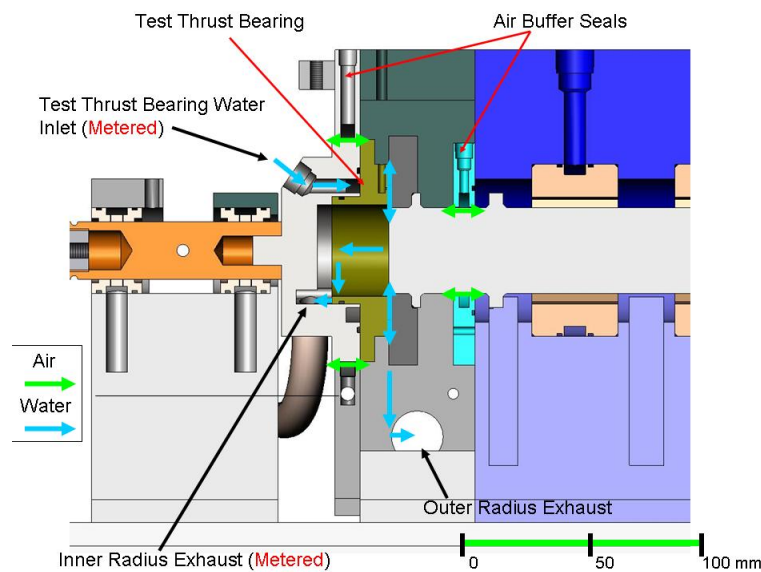


Figure 7: Test thrust bearing and test thrust bearing air seal flow paths

Air buffer seals are also used to seal on either side of the test rig, preventing exhaust-flow leakage.

Flow control to the thrust bearings and the journal bearings was established via three pneumatic control valves. Separate control valves were used for the test thrust bearing, the journal bearings, and the slave thrust bearings. Further details can be seen in the flow schematic in Appendix A.

The test rig is intended for rotational testing of the thrust bearing's characteristics. The rig configuration was also designed with future test programs in mind. For these later test programs, the rig was designed to accept bearings with a range of flange and fluid supply design.

Considerations for testing thrust bearings under dynamic conditions were incorporated. These include the use of air bearings to support the loading shaft to avoid friction losses from the movement of the test thrust bearing and minimizing the mass of the moving assembly that supports the test thrust bearing. Dynamic testing would involve applied measured harmonic excitation using the shaker.

For initial non-rotating testing, the modified configuration shown in Figure 8 was utilized. This configuration allowed for testing without pressurizing both thrust bearings by applying the load at the slave end of the rotor.

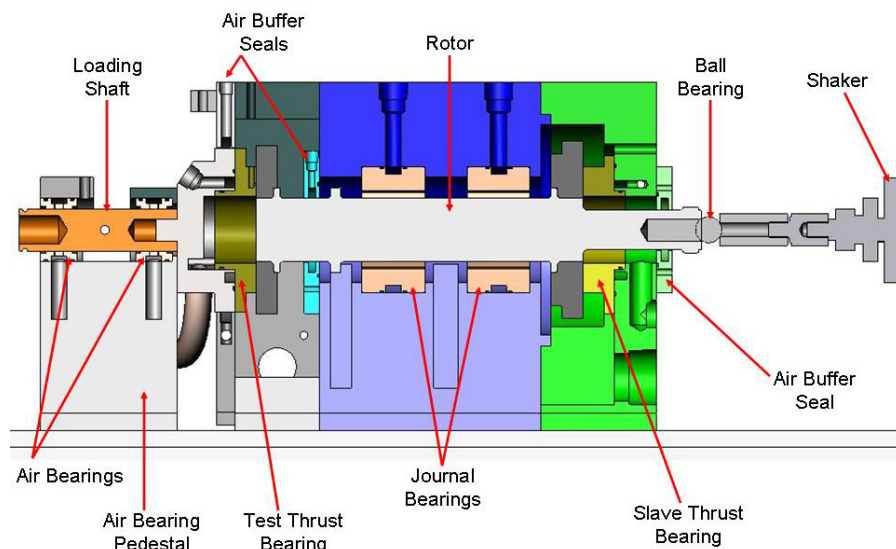


Figure 8: Schematic of hydrostatic thrust bearing test rig non-rotating testing configuration

This configuration simplified the initial testing process by removing the necessity of operating the slave thrust bearing. Thus, alignment issues or other possible problems from the slave thrust bearing did not interfere with the initial tests. The static testing configuration applies load to the rotor directly, which is then reacted by the air bearing pedestal through the test thrust bearing and rotor as shown in Figure 9.

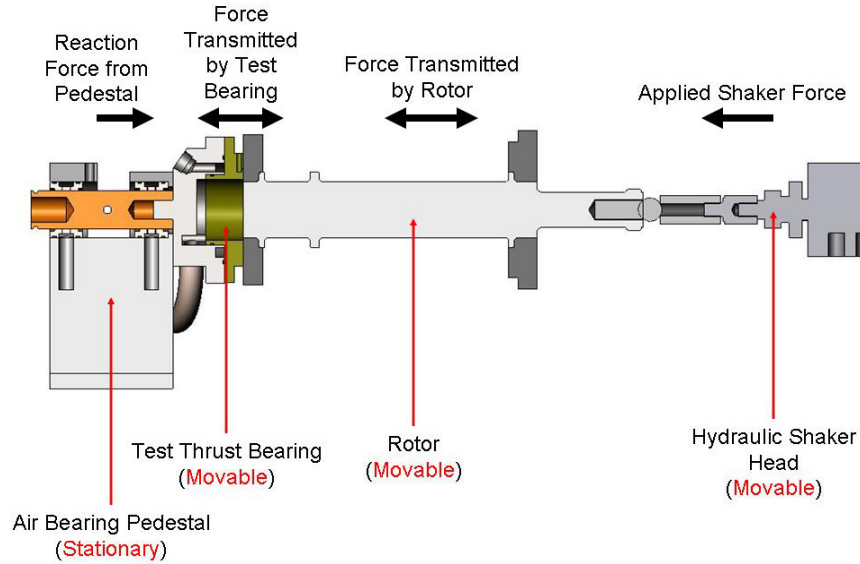


Figure 9: Static configuration load path

During testing, the test thrust bearing is monitored using eddy current proximity probes to determine the operating clearance, flow meters for recording inlet and exit flow, as well as several pressure and temperature measurements.

The thrust bearing is a hydrostatic bearing with eight pockets. Figure 10 shows a front view.

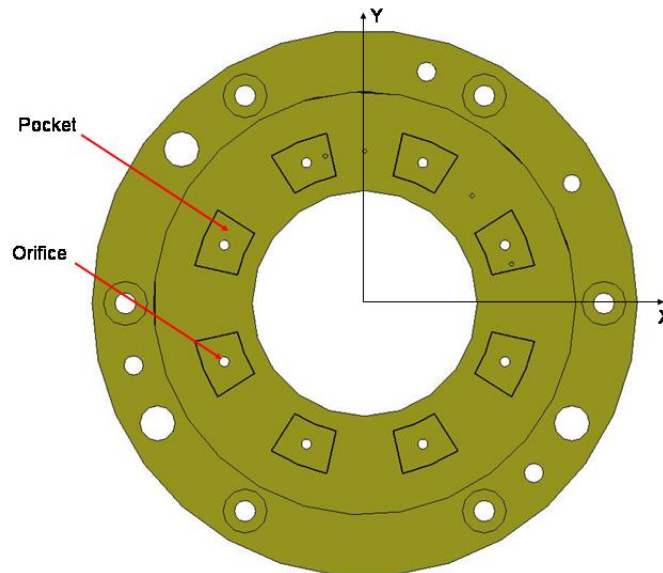


Figure 10: Front view of test thrust bearing

The bearing is designed to mount in the thrust bearing support of the test rig. Table 1 lists the geometric parameters for the thrust bearing.

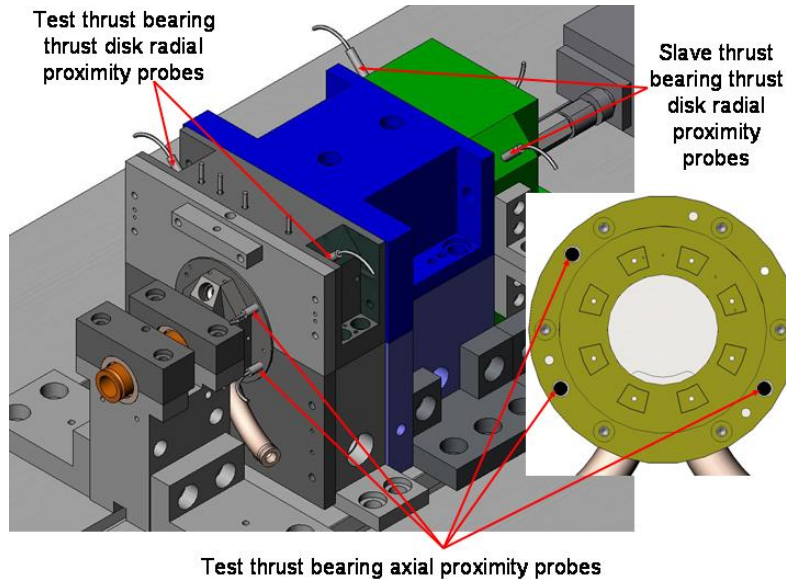
Table 1: Important dimensions and parameters for the tested thrust bearing

Bearing inner radius	20.32 mm (0.80 in)
Bearing outer radius	38.10 mm (1.50 in)
Number of pockets	8, Equally spaced
Pocket arc length	0.349 rad (20°)
Pocket inner radius	23.47 mm (0.924 in)
Pocket outer radius	31.47 mm (1.239 in)
Pocket depth	5.08 mm (0.020 in)
Orifice location	Located at mid-radius and mid-arc of pocket
Orifice diameter	1.80 mm (0.071 in)

The slave thrust-bearing parameters are identical to the test thrust-bearing parameters listed in Table 1. The slave thrust bearing features a different flange design and is thicker due to a split design.

Instrumentation

Four types of instrumentation were required for the non-rotating tests of the hydrostatic thrust bearing: eddy current proximity probes, thermocouples, pressure sensors, and flow meters. Seven proximity probes were used in the static testing configuration. The proximity probe locations are shown in Figure 11.

**Figure 11: Locations of eddy current proximity probes during non-rotating tests**

These proximity probes are used to monitor the rotor position. Two probes are dedicated to monitoring each of the rotor ends' radial position to insure rotor lift off. These probes will also be used during tests with rotor rotation to monitor the rotor radial motions. The remaining three probes are used to monitor the axial position of the test thrust bearing relative to the test bearing thrust disk. Three proximity probes in this application define the thrust bearing face's position relative to the plane of the thrust disk. This capability means that the misalignment of the thrust disk relative to the bearing can be determined. Additional proximity probes will be added to monitor the slave thrust bearing axial position and alignment for rotational testing.

The proximity probe selected was the SKF CMSS-65 5mm system. This system uses a five millimeter diameter probe that attaches to a driver which outputs a voltage to the DAQ. The probe system requires a -24 V power source and outputs a signal from -2 to -20 V [14]. However, the DAQ card requires a signal to be within the ± 10 V range [15]. To correct this discrepancy, Encore model 619M signal conditioners were used to offset the signal and to attenuate it if necessary.

Each proximity probe was calibrated in the same configuration used during testing, including extension cable, probe, and driver. Calibration also used the rotor, the intended probe target, to develop the output curve to assure that the inconel composition did not cause measurement error. Measurements were made of the output voltage from the driver with a digital voltmeter and the probe distance from the rotor using a dial gauge. These readings were then compiled to find the linear region of the probe with the rotor target and the equation of the line through the linear region. An example curve is shown in Figure 12. With the calibration curves, the linear region of the probes with inconel was found to be from 0.4 to 1.5 mm approximately, and the best fit line was found for each probe system.

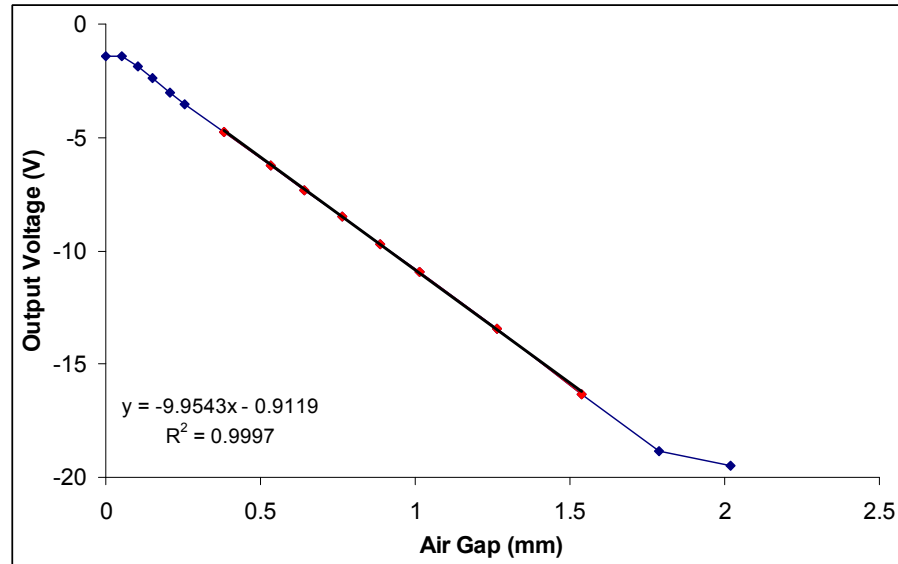


Figure 12: Example calibration curve for an eddy current proximity probe used on the hydrostatic thrust bearing test rig

Four thermocouples were also used. Two thermocouples measured the inlet flow to the test thrust bearing and the journal bearings. Plug-style type-K thermocouples were used to prevent failure at maximum operating pressure. The other two thermocouples were mounted to the inner and outer radius of the test thrust bearing as seen in Figure 13.

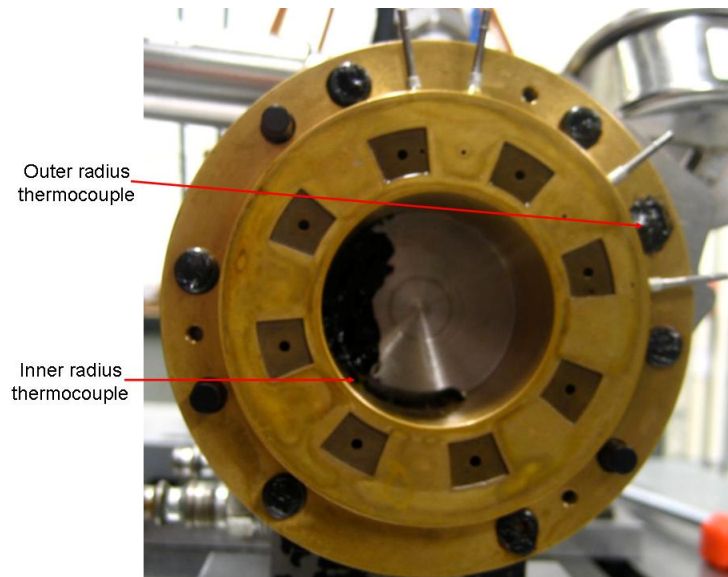


Figure 13: Locations of the inner and outer radius thermocouples on the test thrust bearing

These two thermocouples are type K and are secured in place with silicone to measure the temperature of the flow from the outer radius and inner radius of the test thrust

bearing. All four thermocouples are wired to Omega DP25B displays and were calibrated with the displays using an ice-water and a boiling-water bath. The displays output a 0 to 5 V signal to the DAQ. An additional plug type thermocouple is also installed in the water supply piping to monitor the inlet supply temperature of the slave thrust bearing for testing with rotor rotation.

Seven pressure sensors were used in the non-rotating testing. Figure 14 shows the three sensors used to monitor the inlet pressures to the test thrust bearing and each of the radial bearings.

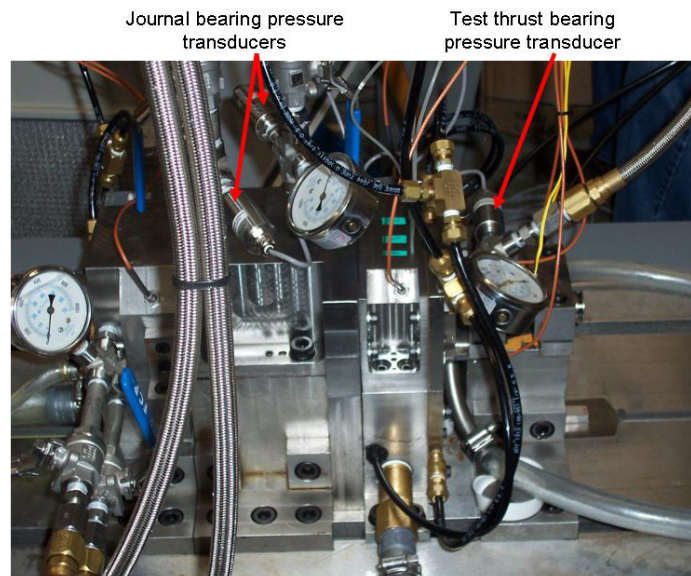


Figure 14: Inlet pressure sensors for journal bearings and test thrust bearing

As shown, the test thrust-bearing supply-pressure sensor and gage were mounted as near as possible to the bearing to provide representative pressure readings. Additionally, the two journal-bearing supply-pressure sensors are used to confirm that both bearings are operating at nearly identical pressures. Two additional pressure transducers will be added to monitor the slave thrust bearing for rotational testing. The remaining four pressure sensors are used to measure the pressures in two of the pockets and at two locations on the lands. Figure 15 shows the pressure tap positions.

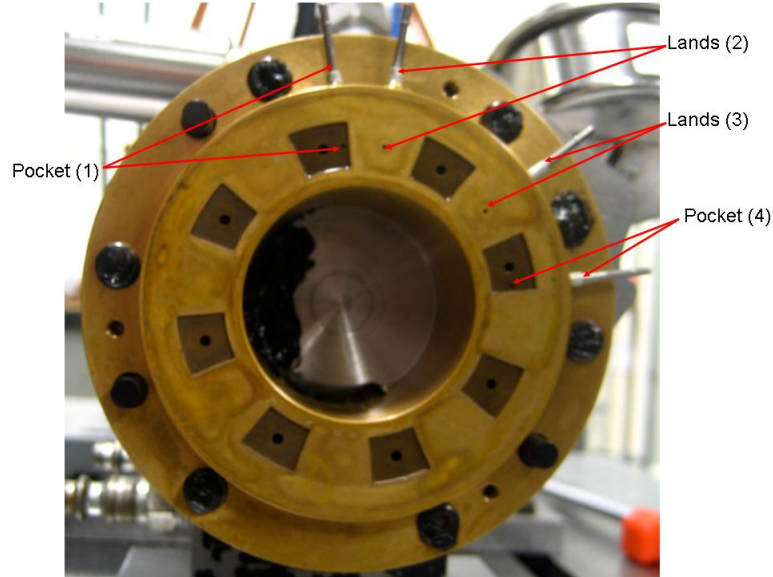


Figure 15: Location of pressure taps for pressure measurement on bearing lands and pockets

The taps in the bearing face intersect with a perpendicular hole which leads to the edge of the bearing. From there, the taps are hooked into their respective static pressure transducers by way of flexible tubing. Each pressure transducer was calibrated with its respective DP-25 display using a dead-weight tester over the range of 0 to 20.7 bar. The analog output from each DP-25 display was then routed to the DAQ.

Finally, three flow meters were used during testing. These flow meters were used to monitor the inlet flow to the journal bearings and the test thrust bearing in addition to the exhaust flow from the inner radius of the test thrust bearing. The location of the flow meters can be found in the flow schematic in Appendix A. All of the flow meter outputs were wired to signal linearizers with output displays. Outputs from the linearizers were then wired into the DAQ.

All data from the testing was collected using a single PCI-6225 DAQ board.

Table 2 contains a summary of the specification for the DAQ board.

Table 2: Table of DAQ board specifications [15]

Board Type	Number of Channels	Sampling Rate (Ksamples/sec)	Resolution (bits)	Signal Range (V)	Signal Type
PCI-6225	80	250	16	± 10	Analog/Digital Input/Output Analog Input used

For additional details on the transducers and their accessories see Appendix B.

Non-Rotating Test Procedure

Testing began after the final assembly of the hydrostatic thrust bearing test rig. The testing was divided into three parts based on the supply pressure range of the thrust bearing at 3.45, 10.34, and 17.24 bar. At each of these pressures, ten loads were selected to span the thrust bearing load capacity as determined by initial predictions from XLHydroTHRUST®.

Alignment difficulties between the thrust bearing and thrust disk face were encountered. This problem arose through a combination of the tolerance stack up involved in the air bearing support, and using the air bearing pedestal as a backstop for the test thrust bearing. Initially, the direct stinger attachment to the rotor was thought to cause the misalignment. This possibility was eliminated using a ball to replace the stinger as an interface between the shaker and rotor as shown in Figure 8.

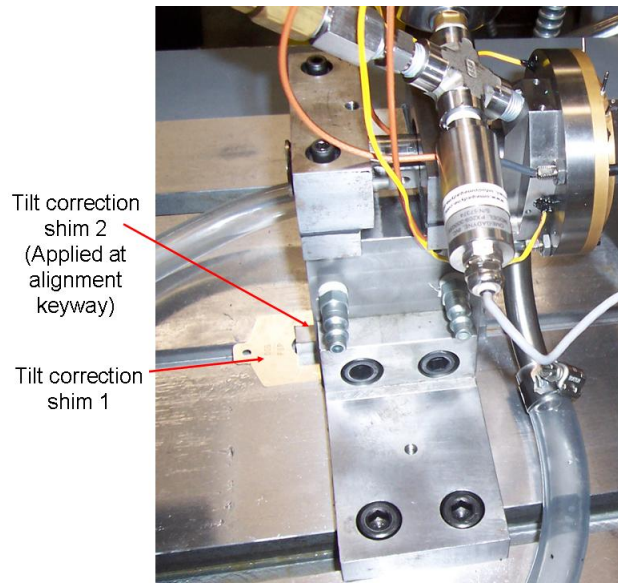


Figure 16: Tilt adjustment shims for the correction of test thrust bearing tilt in static testing configuration

The problem was solved by shimming the air bearing pedestal. Application of shims at the locations noted in Figure 16 on the air bearing pedestal moved the entire support pedestal to correct the observed misalignment measured during tilt assessment testing. Misalignment was corrected in two directions from the combination of the following two shims: (1) about the horizontal axis of the thrust bearing by “shim 1” located under the pedestal, and (2) about the vertical axis by “shim 2” placed in with the

alignment keyway. With these shims, the misalignment between the thrust bearing face and thrust disk was decreased to 0.013 mm or less for all test cases.

The correction shimming was determined based upon the misalignment slopes of the test bearing in relation to the thrust disk. The formula for the misalignment slope in the horizontal x direction (M_1) is shown in Equation (1.1), and the misalignment slope in the vertical y direction (M_2) is shown in Equation (1.2).

$$M_1 = 0.00194(Z_2 - Z_3) \quad (1.1)$$

$$M_2 = (-0.00294Z_1 + 0.00277Z_2 + 0.00017Z_1) \quad (1.2)$$

Where

M_1 = Misalignment in the x direction $\left(\frac{\text{mm}}{\text{mm}}\right)$

M_2 = Misalignment in the y direction $\left(\frac{\text{mm}}{\text{mm}}\right)$

Z_1, Z_2, Z_3 = Gap reading from probe 1, 2, or 3

The derivation for the misalignment slopes can be found in Appendix C. These slopes were used with the length of the pivot (the length of the air bearing pedestal) to determine the correction shim dimension.

After several tests, the misalignment was determined to be load dependent, most likely due to the use of the air bearing pedestal as a backstop. Hence, before each test, a tilt assessment test (TAT) was performed over a test load range. The TAT was usually performed with three loads which were then used to calculate the correction shim dimension. For the 3.45 bar tests, one correction was adequate while for the 10.34 and 17.24 bar tests, three and five corrections were necessary, respectively, to cover the entire load range.

Each shim set reduced the misalignment of the thrust bearing face relative to the rotor to approximately 0.013 mm in the x and y directions across the entire thrust bearing face. This misalignment limit was determined by the length of the bearing pedestal where the adjustment was made and the thickness of the available shims. With a longer bearing pedestal or a smaller adjustment method, the misalignment tolerance could be reduced.

When the tilt corrections were complete, data were collected. Fifteen data points were collected for each 3.45 and 10.34 bar supply pressure load. This was increased to twenty data points for each 17.24 bar supply pressure load.

Non-Rotating Test Results

After the tests, the collected data needed to be compared to predictions from XLHydroTHRUST®. For more accurate predictions, the orifice discharge coefficient was extracted from the collected data. Equation (1.3) [16] shows the equation used to calculate the discharge coefficient (C_d).

$$C_d = \frac{Q_0}{A_0 \sqrt{\frac{2}{\rho} (P_s - P_R)}} \quad (1.3)$$

Where

A_0 = Area of the orifice (m^2)

C_d = Orifice discharge coefficient

P_R = Recess (pocket) pressure (Pa)

P_s = Supply pressure (Pa)

Q_0 = Flow rate through an orifice (m^3/s)

ρ = Working fluid density (kg/m^3)

The equation assumes that the pocket pressures are all equal to the measured average pocket pressure and that the flow through each orifice is equal. This assumption is necessary due to the measurements taken that cannot isolate any specific orifice, forcing the average assumption. Figure 17 shows the derived orifice coefficients for the three test supply pressures.

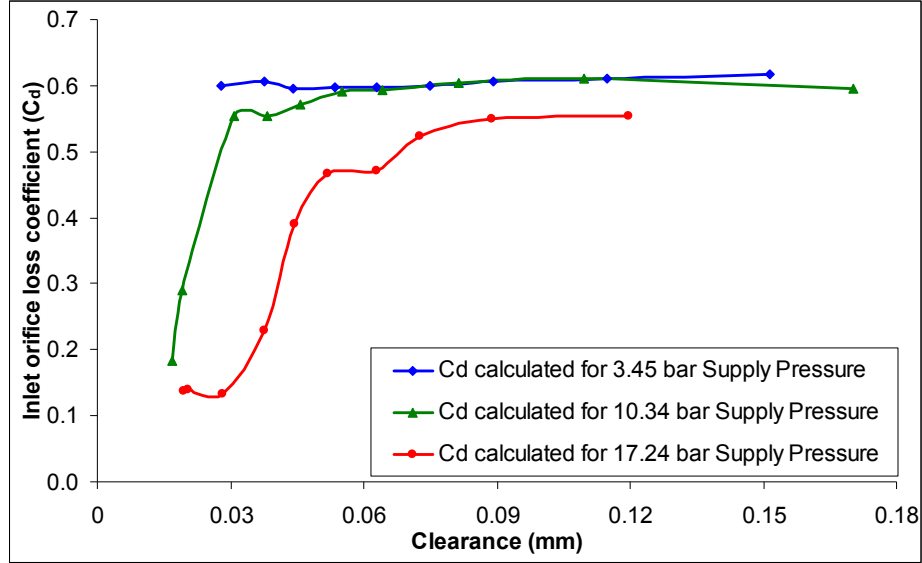


Figure 17: Orifice loss coefficient calculated from test data for 3.45, 10.34, and 17.24 bar test thrust bearing supply pressure tests

This figure shows that the orifice discharge coefficient is nearly constant over selected clearances for the 3.45 bar case. However, with the higher bearing supply pressures, decreased clearances are reached where the orifice discharge coefficient drop to lower values. This decrease appears to stabilize for the 17.24 bar thrust bearing supply pressure at a discharge coefficient of approximately 0.15. The 10.34 bar case though does not reach this relatively constant second range, and the 3.45 bar case shows no decrease in the orifice discharge coefficient. To examine this result, the orifice Reynolds number is calculated from

$$Re_{Orifice} = \frac{\rho * V_{Orifice} * D_{Orifice}}{\mu}$$

Where

$Re_{Orifice}$ = Orifice Reynolds number

ρ = Working fluid density $\left(\frac{\text{kg}}{\text{m}^3}\right)$ (1.4)

$V_{Orifice}$ = Fluid velocity through orifice $\left(\frac{\text{m}}{\text{s}}\right)$

$D_{Orifice}$ = Diameter of the inlet orifice (m)

μ = Dynamic viscosity $\left(\frac{\text{N}\cdot\text{s}}{\text{m}^2}\right)$

The orifice Reynolds number is shown in Figure 18.

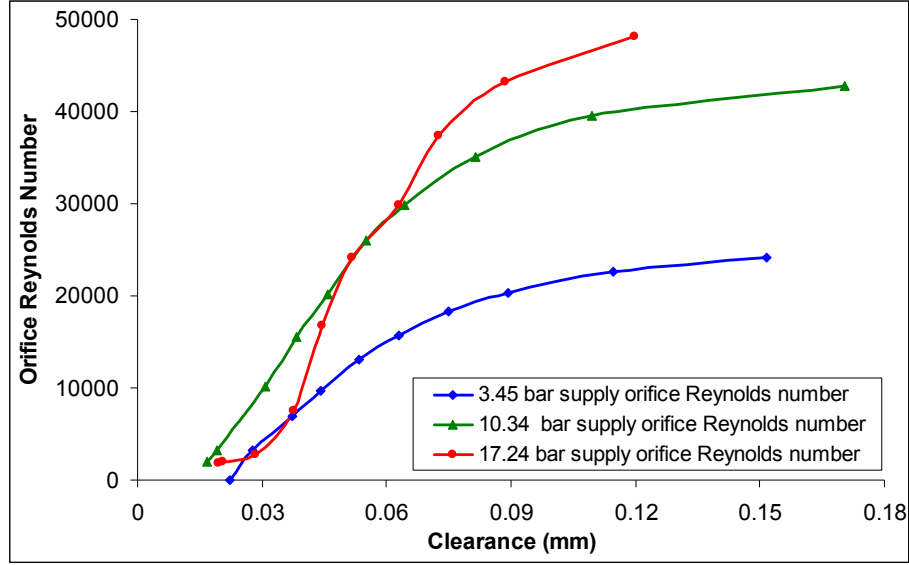


Figure 18: Orifice Reynolds number calculated from test data for 3.45, 10.34, and 17.24 bar test thrust bearing supply pressure tests

Figure 18 indicates that the orifice Reynolds number transitions from laminar to turbulent over the test range. Munson et al. [10] shows that the discharge coefficient can change with the Reynolds number until it is well into the turbulent regime; however, the orifice loss coefficient increases in Munson et al [10], disagreeing with the present calculated coefficients. The Reynolds number at the thrust bearing outer radius is next checked in Equation (1.5).

$$Re_{OuterRadius} = \frac{\rho * V_{OuterRadius} * Z}{\mu}$$

Where

$Re_{OuterRadius}$ = Outer radius Reynolds number

ρ = Working fluid density $\left(\frac{\text{kg}}{\text{m}^3}\right)$

$V_{OuterRadius}$ = Average fluid velocity through thrust bearing outer radius $\left(\frac{\text{m}}{\text{s}}\right)$

Z = Center clearance of thrust bearing (m)

μ = Dynamic viscosity $\left(\frac{\text{N}\cdot\text{s}}{\text{m}^2}\right)$

(1.5)

The outer radius Reynolds number is shown in Figure 19.

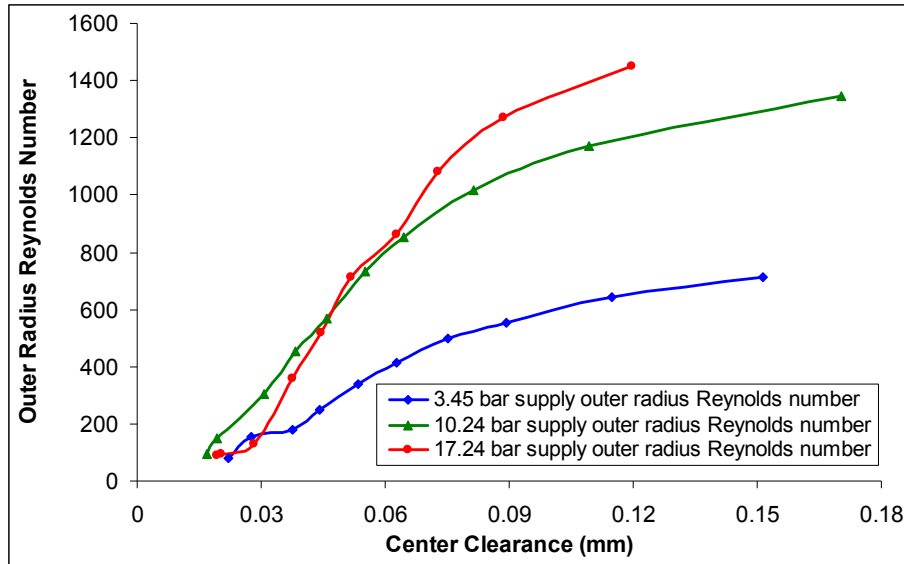


Figure 19: Outer radius Reynolds number calculated from test data for 3.45, 10.34, and 17.24 bar test thrust bearing supply pressure tests

This Reynolds number indicates laminar flow through all tests, which does not explain the change in the orifice loss coefficient. Neither of these Reynolds-number plots explains the observed change in the discharge coefficient. This change may relate to the misalignment across the bearing face, but further data would be necessary to show this.

For XLHydroTHRUST® predictions, a constant orifice discharge coefficient is required. For this purpose an average value was taken at the stable high clearance value. This average is not entirely accurate for the smaller clearances but is an adequate approximation over the entire range for comparison with hypothetical predictions. The averaged values used for the orifice discharge coefficient are shown in Table 3.

Table 3: Average orifice discharge coefficients used for XLHydroTHRUST® predictions

Thrust Bearing Supply Pressure (bar)	Average orifice discharge coefficient
3.45	0.61
10.34	0.61
17.24	0.51

Additionally, the static misalignment angles about each axis, in radians, were required for the XLHydroTHRUST® predictions. These misalignments were found from the M_1 and M_2 slopes of Equations (1.1) and (1.2). They were converted to misalignment in radians by using the slope in $\frac{\text{mm}}{\text{mm}}$ and taking the inverse tangent function. Because of

the small angle, the resulting angle was approximately the slope in $\frac{\text{mm}}{\text{mm}}$. Figure 20 shows the misalignments for the three supply pressure tests.

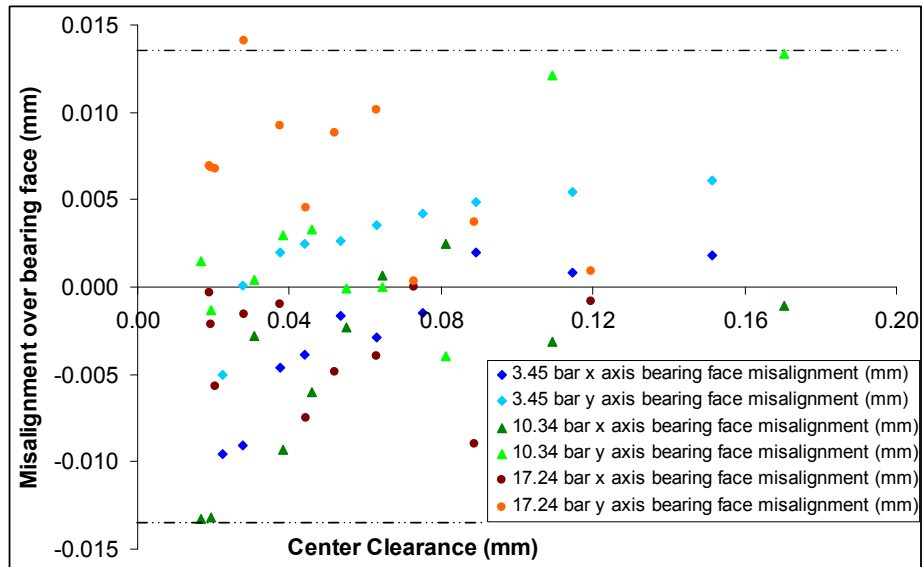


Figure 20: Misalignment over the bearing face about the x and y axis for 3.45, 10.34, and 17.24 bar test thrust bearing supply pressure test. Lines mark desired limits for misalignment ± 0.013 mm

This figure shows that tests were performed at reasonably low misalignment values for all cases. For the majority of the points, the misalignment was maintained within the targeted range of ± 0.013 mm over the bearing face, indicated by the marker lines on Figure 20, with the few outliers missing the maximum limit by a small amount. For low clearances, smaller misalignments are desirable, but due to correction limitations were not attainable. For more detailed figures of the misalignment for each supply pressure see Appendix D.

Finally, the temperature of the inlet water was determined from an average of the recorded water inlet temperatures. With these parameters, XLHydroTHRUST® was used to predict the thrust bearing behavior. These predictions were then compared to the acquired test data.

Figure 21 shows the measured flow rates into the thrust bearing and out through the inner radius.

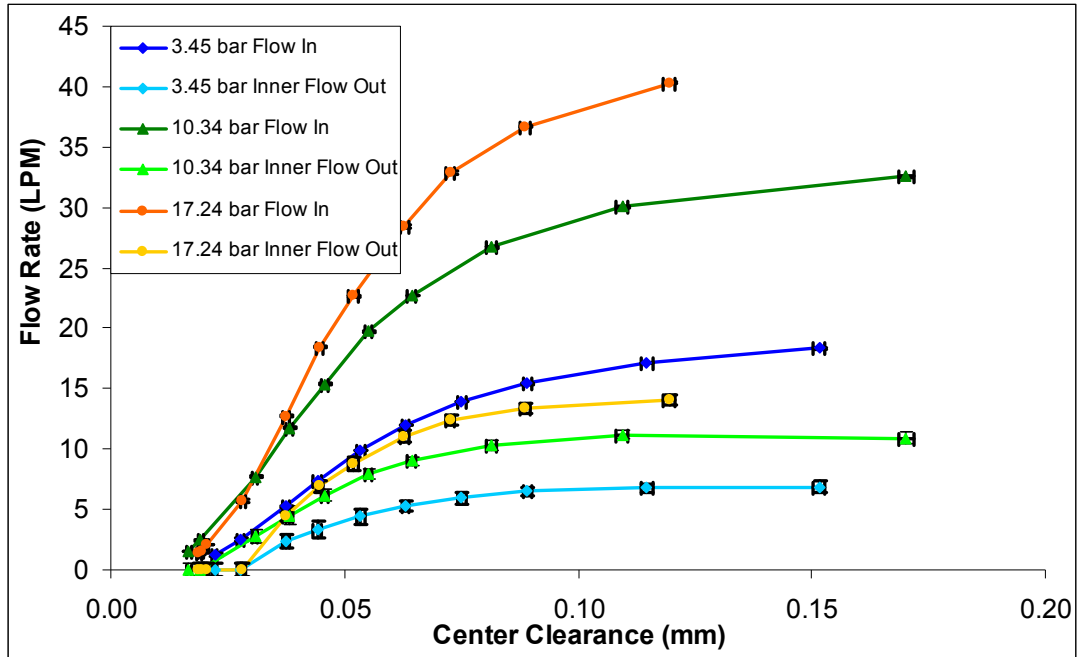


Figure 21: Measured inlet flow rates and flow out through inner radius of thrust bearing for 3.45, 10.34, and 17.24 bar thrust bearing supply pressures with uncertainty bars shown.

All uncertainty bars are shown on the plot but are barely noticeable. For details on the uncertainty calculations of the flow rate and the other experimental measurements see Appendix E. The uncertainty of the inlet flow measurement is around 1% or less. The uncertainty of the inner radius out flow is larger but near or less than 5%.

Figure 22 shows both the predictions and the measurements of the inlet flow rate.

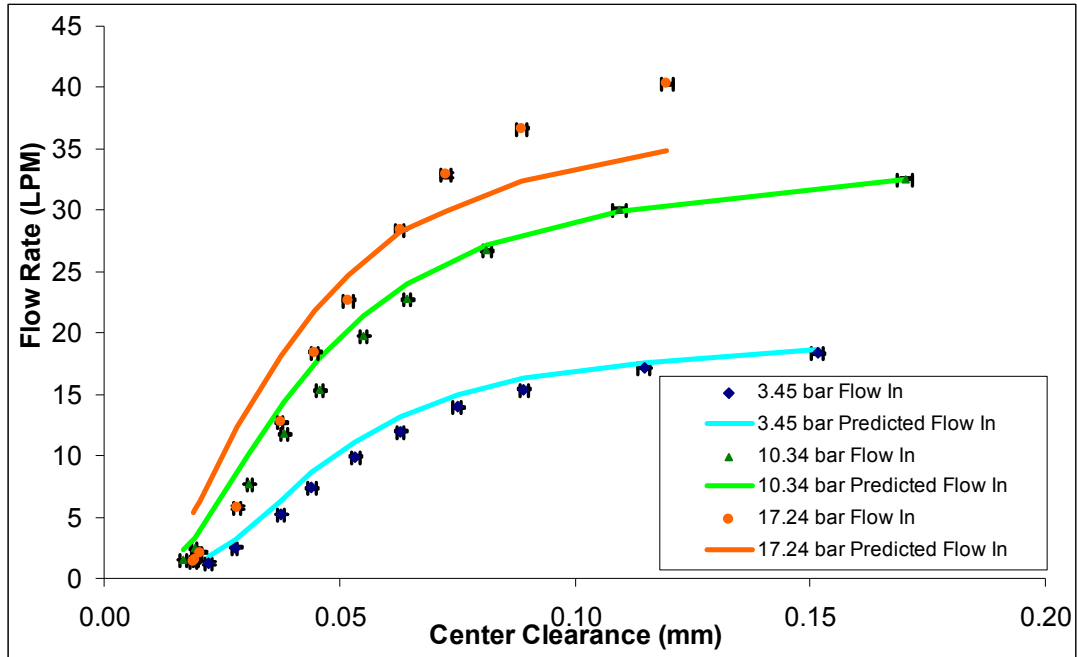


Figure 22: Measured and predicted inlet flow rates for 3.45, 10.34, and 17.24 bar supply pressures.

This figure shows that the correlation between the predictions and measurements is very good for the 3.45 and 10.34 bar cases but poorer for the 17.24 bar case. The 3.45 and 10.34 bar case predictions generally match the measurements within 20% with the exceptions occurring for the very low flow rates. The 17.24 bar case predictions had differences that were mostly near 20%. The error between the measurements and the 17.24 bar predictions was also significantly over 20% for the data collected at the lowest five clearances. The poorer correlation of the 17.24 bar case is likely due to the more variable orifice loss coefficient which is shown in Figure 17. This causes a less accurate set of predictions from XLHydroTHRUST®, which assumes a constant orifice loss coefficient. All predictions show the general trends observed in the experimental measurements. Figure 23 compares measured flow rates exiting from the inner radius of the bearing plotted with the predictions obtained from XLHydroTHRUST®.

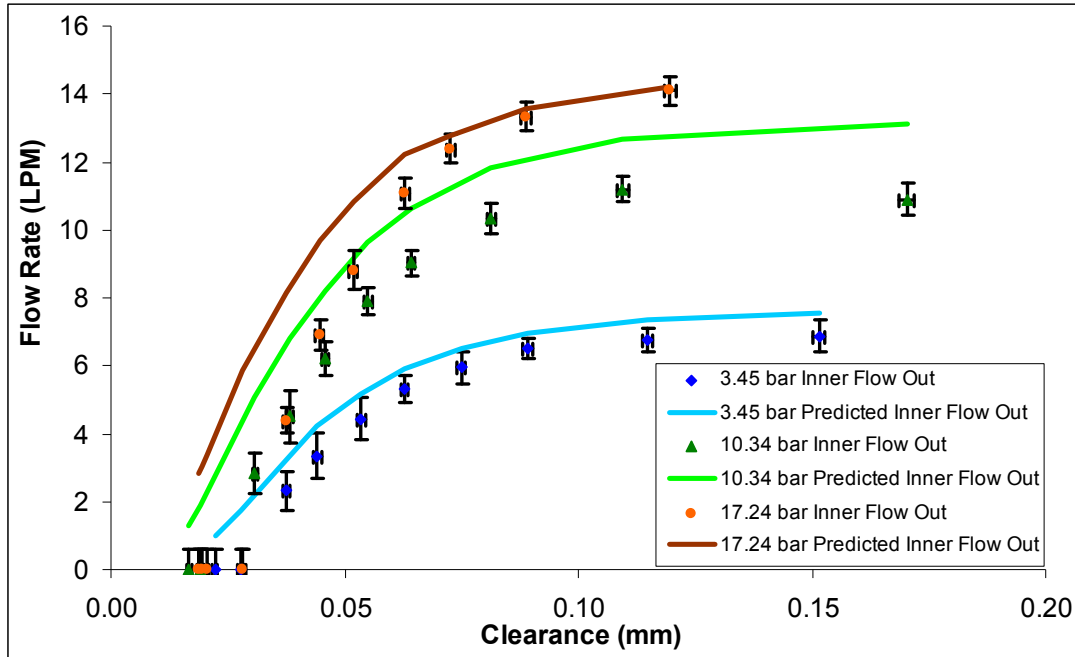


Figure 23: Measured exhaust flow rate through the inner thrust bearing radius and predictions from XLHydroTHRUST®. Flow rates plotted for 3.45, 10.34, and 17.24 bar.

The measurements and predictions in Figure 23 show poorer correlation than those for the inlet flow rate with nearly twice the error between measurements and predictions for the majority of points. The best correlation occurs for the 3.45 and 10.34 bar supply pressure cases where the prediction appear to be offset slightly for the entire range of measured values. Additionally, for the majority of the measured range, the 3.45 bar predictions fall within the error of the measurement of the inner radius flow rate. The 17.24-bar measurements show a significantly higher decrease in flow rate with decreasing clearance than predicted. This is probably related to the large drop off in the discharge coefficient seen in Figure 17.

The calculated differences between the measurements and the XLHydroTHRUST® predictions are calculated using

$$\% \text{ Difference} = \frac{|\text{Measured Value} - \text{Predicted Value}|}{\text{Measured Value}} * 100 \quad (1.6)$$

The resulting errors are reasonable for all supply pressures with a clearance greater than 0.05 mm. The predicted inlet flow remains within approximately 10% of the measured

value, and the predicted exhaust flow of the inner radius remains within 20% of the measured value in this range. For clearances less than 0.05 mm, the error increases significantly though this may also be due in part to the increased significance of the bearing face on the orifice loss coefficient.

The next parameter compared is the pocket pressure ratio defined in Equation (1.7).

$$P_{Ratio} = \frac{P_{Pocket} - P_{Exhaust}}{P_{Supply} - P_{Atmospheric}}$$

Where

P_{Ratio} = Pressure ratio

P_{Pocket} = Pocket pressure

$P_{Exhaust}$ = Pressure bearing exhausts into

P_{Supply} = Supply pressure

$P_{Atmospheric}$ = Atmospheric pressure

(1.7)

Figure 24 shows the pocket pressure ratios over the tested clearance range for the tested supply pressures.

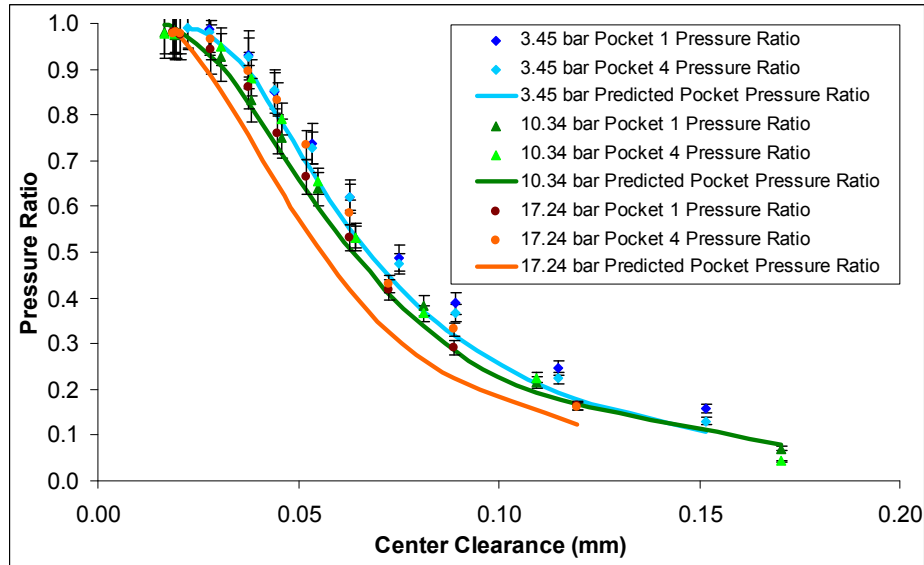


Figure 24: Pocket pressure ratios over the tested clearance range for 3.45, 10.34, and 17.24 bar thrust bearing supply pressure.

Figure 24 shows that the pocket-pressure ratio for the supply pressures ranges from a low value, ~0.05 for 3.45 bar to ~0.15 for 17.24 bar to approximately 1. These results indicate that most of the useful load range of the thrust bearing was covered in testing.

This figure also shows that the pocket 1 and pocket 4 pressure ratios are nearly identical over the tested range, providing another check that the test thrust bearing and rotor thrust disk misalignment is low. The predictions also match closely for the 3.45 and 10.34 bar supply pressures. The 17.24 bar case predictions are low by approximately 15-25% of the measured value at clearances greater than 0.028 mm. Below this clearance the pressure ratio compares well for this supply pressure. Pressures from the lands were also collected, but the data appeared anomalous at higher pressures. This discrepancy is attributed to a leak in the tube from the pressure taps to the pressure sensor. Thus the pressure data from the lands was considered invalid. For more detailed figures of the pocket pressures for each supply pressure see Appendix D.

Figure 25 depicts the loading behavior of the thrust bearing over the tested clearance range.

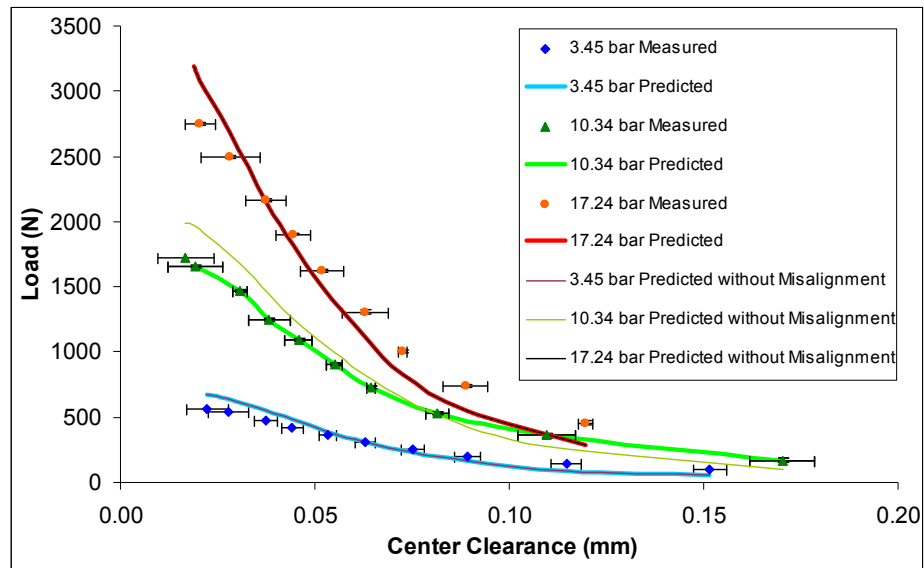


Figure 25: Experimentally measured test thrust bearing clearance versus load and XLHydroTHRUST® predictions with and without misalignment

All three plots show similar trends to those in San Andres [12] as well as in Wang and Yamaguchi [6]. The figure also shows that the predictions are in reasonable agreement with measurements. Predictions correlate especially well with the 10.34 bar measurements. Experimental errors are also shown in the plot. The load uncertainties shown are small and do not significantly alter the data with their inclusion. The clearance uncertainties are larger due to the inclusion of the tilt in the uncertainty bar to show the

clearance range over the entire bearing face. Predictions for the 3.45 and 17.24 bar supply pressure case show little difference with misalignment. The 10.34 bar supply pressure case does show some change with the addition of the misalignment.

Percentage errors between the experimental data and the predictions are calculated using Equation (1.6). Predictions remain within approximately 20% of the measured values for clearances less than 0.09 mm in all cases. Higher clearances show significantly higher errors. However, these errors confirm that the 10.34 bar predictions correlate best overall with the measurements.

The stiffness predictions from XLHydroTHRUST® cannot be directly compared to results extracted from to date measurements. An estimation of the inverse flexibility can be made though. Equation (1.8) shows the flexibility equation.

$$\begin{bmatrix} f_{FF} & f_{FM\Phi_x} & f_{FM\Phi_y} \\ f_{M\Phi_x F} & f_{M\Phi_x M\Phi_x} & f_{M\Phi_x M\Phi_y} \\ f_{M\Phi_y F} & f_{M\Phi_y M\Phi_x} & f_{M\Phi_y M\Phi_y} \end{bmatrix} \begin{bmatrix} F_z \\ M_{\Phi_x} \\ M_{\Phi_y} \end{bmatrix} = \begin{bmatrix} Z \\ \Phi_x \\ \Phi_y \end{bmatrix} \quad (1.8)$$

where

F_z = Load on bearing face

M_{Φ_x} = Moment acting in "a"

f_{mn} = Flexibility coefficient for direction "m" from variable "n"

Z = Thrust bearing clearance

Φ_c = Misalignment angle about axis "c"

The flexibility matrix can be inverted to determine an expression for the force on the bearing. To estimate the inverse flexibility in respect to the bearing clearance the clearance versus load curve can be differentiated.

To estimate the inverse flexibility of the test thrust bearing over the load range the load-versus-clearance data seen in Figure 25 was curve fitted. A fourth-order polynomial was used to fit the data for each load series with the exception of the 10.34 bar case where a third order curve fit was used for higher clearances. These were the lowest order polynomials that would successfully capture the behavior of both the clearance versus load curve and the inverse flexibility curve. Figure 26 shows the 3.45 bar experimental data with a fourth order curve fit equation displayed.

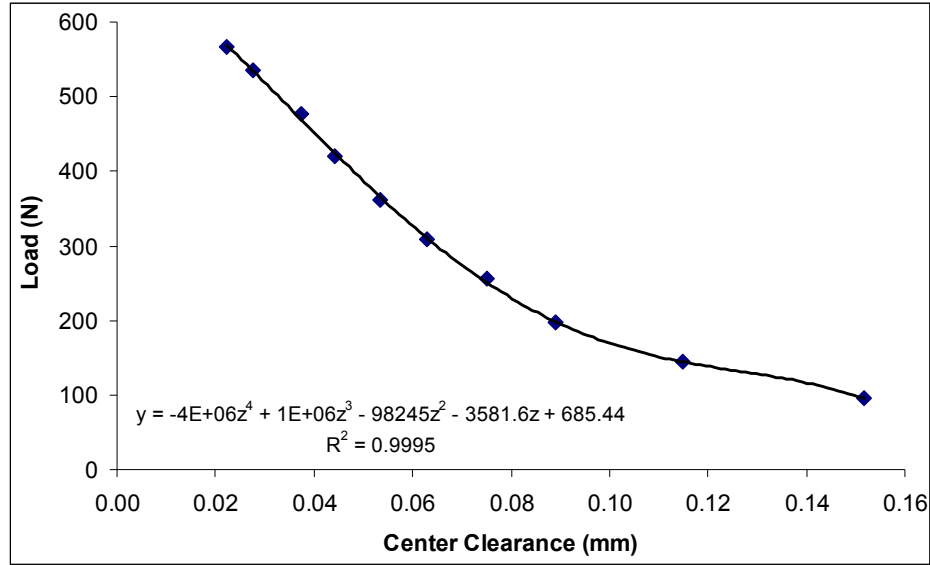


Figure 26: Clearance versus load measurements with fourth order polynomial curve fit for 3.45 bar test thrust bearing supply pressure. Curve fit equation shown.

The plot confirms that the fourth-order curve fits the data well over the data range. With the data in this figure, the thrust bearing axial inverse flexibility can be estimated by taking the curve-fit equation and differentiating. The uncertainty of the inverse flexibility estimation is also a significant parameter. To determine this uncertainty Equation (1.9) was used.

$$E_{dF/dZ} = \sqrt{E_A^2 + E_B^2 + E_C^2 + E_D^2} \quad (1.9)$$

Where

$$Load = A * Z_C^4 + B * Z_C^3 + C * Z_C^2 + D * Z_C + E$$

E_N = Uncertainty associated with term N

Z_C = Thrust bearing clearance

The uncertainty from each term of the curve fit was found using the TableCurve2D program. This program provided a means to check the curve fits from Excel and gave an uncertainty associated with each of the terms. Figure 27 shows curve fit differentiation estimation, or overall inverse flexibility dF/dZ .

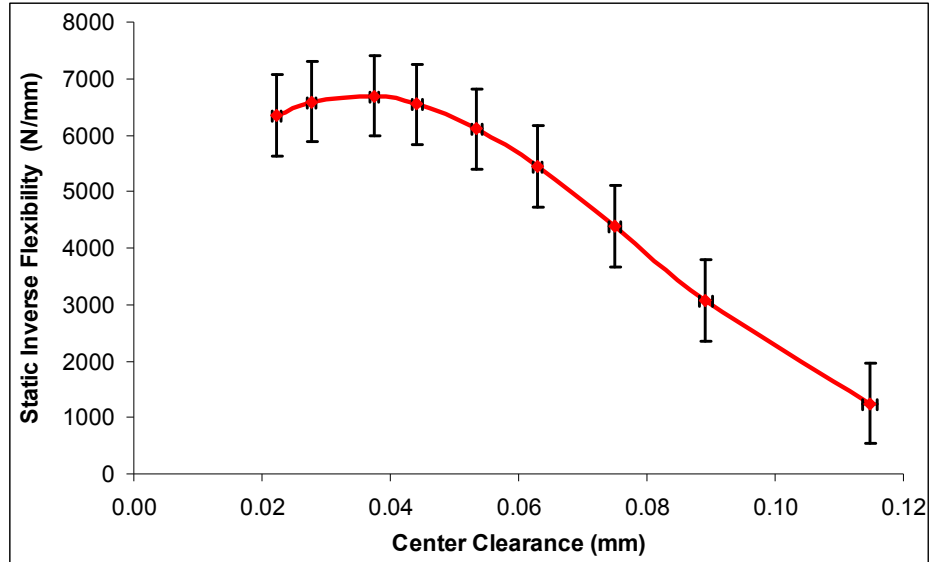


Figure 27: Estimated clearance versus axial inverse flexibility for 3.45 bar test thrust bearing supply pressure

The uncertainty of the differentiation estimation shown in this figure appears reasonable and for the majority of the estimation the uncertainty is approximately 15% or less.

Figure 28 shows the 10.34 bar experimental data with a fourth order and a cubic curve fit.

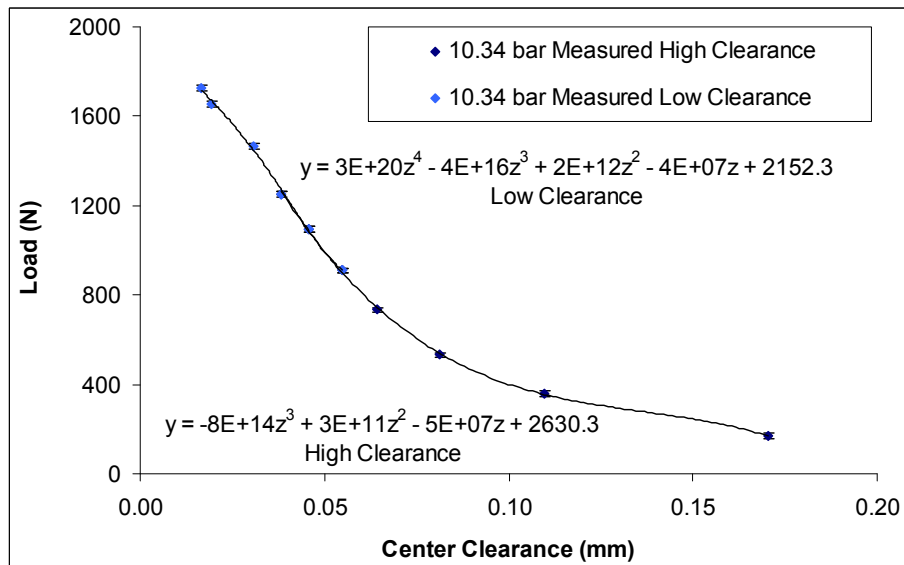


Figure 28: Clearance versus load measurements with two fourth order polynomial curve fit for 10.34 bar test thrust bearing supply pressure. Curve fit equations shown.

This clearance versus load series was split into two parts, due to poor curve fitting results when attempting to fit the entire series. Thus, for the 10.34 bar supply pressure range, a high clearance and low clearance fit were established. These curve fits were used to find the axial inverse flexibility estimates with the same methods used for the 3.45 bar case.

Figure 29 shows the resulting estimates with the XLHydroTHRUST® predictions.

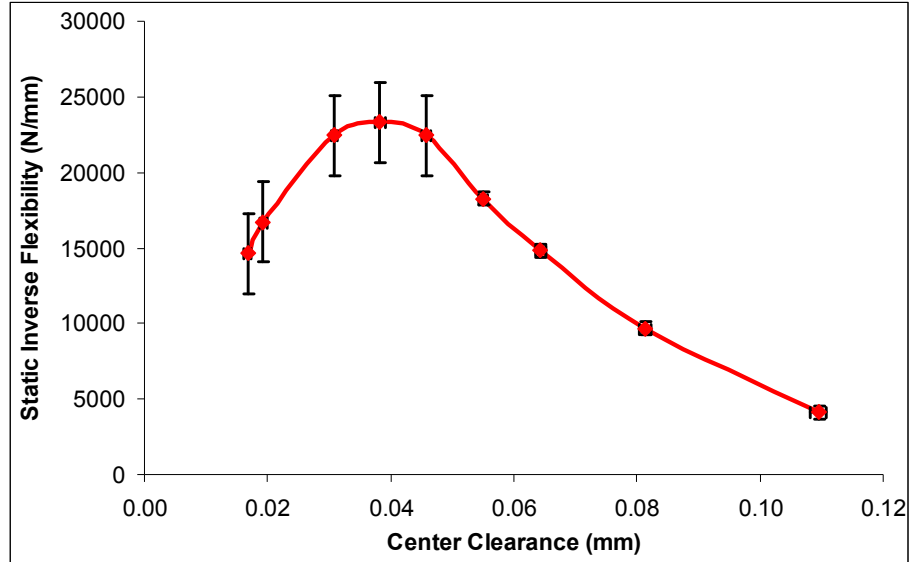


Figure 29: Estimated clearance versus axial inverse flexibility for 10.34 bar test thrust bearing supply pressure

The uncertainty of the differentiation estimation shown in Figure 29 appears good with the majority of the points having an uncertainty less than 10 %.

Figure 30 shows the clearance versus load for the 17.24 bar case with a fourth-order polynomial curve fit.

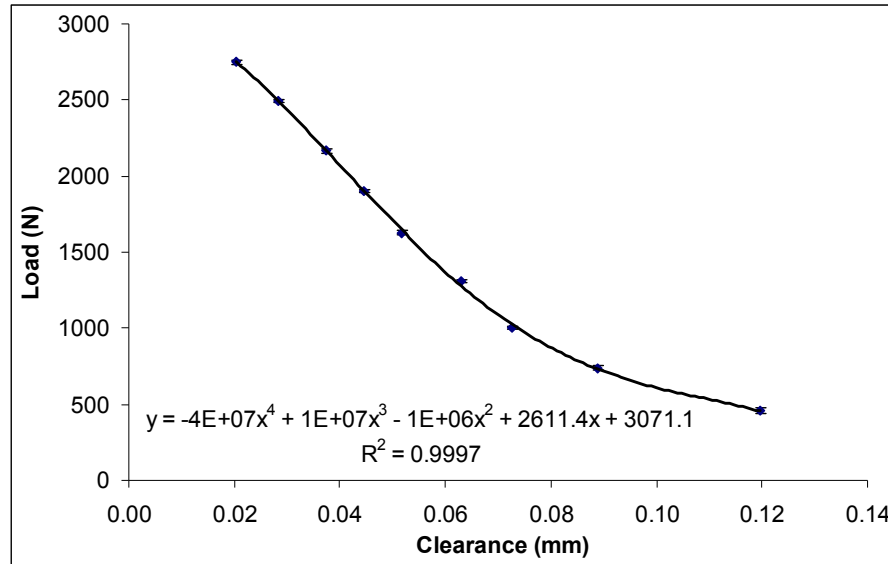


Figure 30: Clearance versus load measurements with two fourth order polynomial curve fit for 17.24 bar test thrust bearing supply pressure. Curve fit equation shown.

A single fourth order polynomial was used to curve fit this clearance versus load data. The curve fit and data points were used as previously. Figure 31 shows predicted and estimated inverse flexibility.

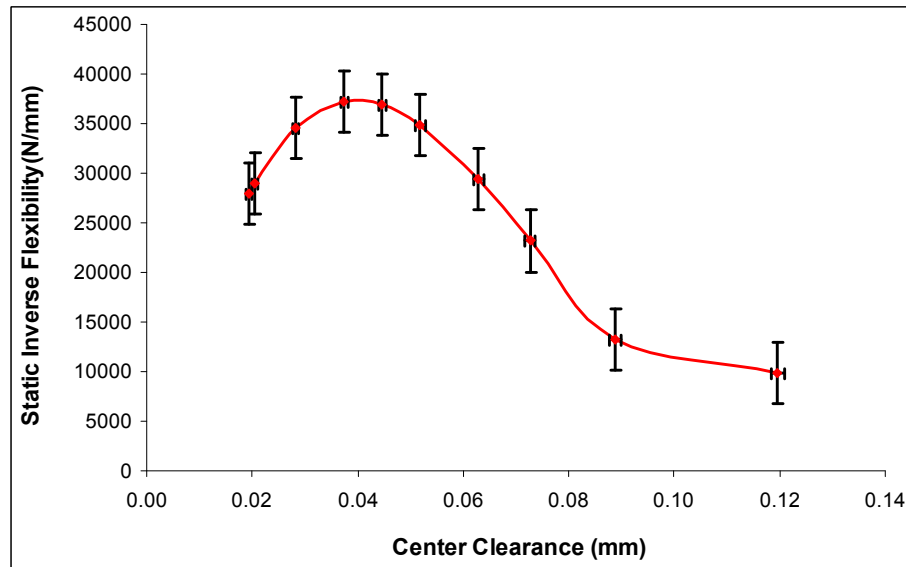


Figure 31: Estimated clearance versus axial inverse flexibility for 17.24 bar test thrust bearing supply pressure

The uncertainty of the differentiation estimation is shown in Figure 31: Estimated clearance versus axial inverse flexibility for 17.24 bar test thrust bearing supply pressure

also appears reasonable with the majority of the points having an uncertainty less than 15 %.

Conclusions

A face-to-face style test rig was designed and built for testing hydrostatic thrust bearings. Using this test rig a hydrostatic thrust bearing was tested under non-rotating conditions. These test results were compared to predictions for flow rate and load from the XLHydroTHRUST® program. The inverse flexibility was also estimated. Predictions correlated reasonably well for flow and load. Stiffness predictions did not compare as well with the measured slopes. The inverse flexibility predictions showed significantly higher maximum inverse flexibilities and much more severe drop offs from this maximum inverse flexibility.

The differences between predictions and measurements may be due to the observed discharge-coefficient variation and thrust bearing face misalignment at low clearance. This discharge coefficient must be given a constant value for XLHydroTHRUST®, but significant changes were observed when extracted from the test data. Further investigation may be warranted to account for this discrepancy.

References

- [1] New, N. H., 1974, "Experimental comparison of Flooded, Directed, and Inlet Orifice Type of Lubrication for a Tilt Pad Thrust Bearing." *Journal of Lubrication Technology*, **96** (1), pp 22-27.
- [2] Gregory, R. S., 1974, "Operating Characteristics of a Fluid-Film Thrust Bearing Subjected to High Shaft Speeds." *Journal of Lubrication Technology*, **96** (1), pp 7-14.
- [3] Neal, P. B., 1982, "Heat Transfer in Pad Thrust Bearings." *Proceedings of the Institution of Mechanical Engineers*, **196** Sept, pp 217-228.
- [4] Horner, D., Simmons, J. E. L., and Advani, A. D., 1986, "Measurements of Maximum Temperature in Tilting-Pad Thrust Bearings." *ASLE Preprints* pp 1-10.
- [5] Harada, Masami, Miyaji, Ryutaro and Anada, Yukio. 1987, "Turbulent Lubrication for a Hydrostatic Thrust Bearing with a Circular Recess." *JSME International Journal*, **30**(269), pp 1819-1825.
- [6] Wang, X. and Yamaguchi, A., 2002, "Characteristics of Hydrostatic Bearing/Seal Parts for Water Hydraulic Pumps and Motors. Part 1: Experiment and Theory." *Tribology International*, **35** (7), pp 425-433.
- [7] Gardner, W. W., 1975, "Performance Tests on Six-Inch Tilting Pad Thrust Bearings." *Journal of Lubrication Technology*, **97** (3), pp 430-438.
- [8] Glavatskih, S. B. 2002. "Laboratory Facility for Testing Hydrodynamic Thrust Bearings." *Journal of Engineering Tribology*, **216** (2), pp 1-12
- [9] Glavatskih, S. B. and DeCamillo, S. 2004. "Influence of Oil Viscosity Grade on Thrust Pad Bearing Operation." *Journal of Engineering Tribology*, **218** (5), pp 401-412
- [10] Munson, Bruce R., Young, Donald F., and Okiishi, Theodore H. 2002. "Fundamentals of Fluid Mechanics." John Wiley & Sons. pp 513-516.
- [11] Rowe, W. B. 1983, "Hydrostatic and Hybrid Bearing Design." Buttersworth & Co. Ltd.
- [12] San Andres, Luis. 2000, "Bulk Flow Analysis of Hybrid Thrust Bearings for Process Fluid Applications." *Journal of Tribology*, **122** (1), pp 170-180
- [13] San Andres, Luis. 2006, "Effects of Misalignment on Turbulent Flow Hybrid Thrust Bearings." *Journal of Tribology*, **124** (1), pp 212-219

- [14] SKF “Eddy Probe Systems Catalog” pg 5-8 October 20, 2007
<<http://www.stiweb.com/downloadDataSheets/eddyprobe.pdf>>.
- [15] National Instruments “Low-Cost M Series Multifunction DAQ – 16-Bit, 250 kS/s, up to 80 Analog Inputs” October 20, 2007.
<<http://www.ni.com/pdf/products/us/20044546301101dlr.pdf>>.
- [16] San Andres, Luis. 2006. “MEEN 626 Notes 12 Annular Seals and Hydrostatic Journal Bearings.” Pg 17
<http://phn.tamu.edu/me626/Notes_pdf/Notes12_Seals_HJBs.pdf>
- [17] Stewart, James. 1998. “Calculus: Concepts and Contexts.” Brooks/Cole Publishing Company. pp 675-682.
- [18] Coleman, Hugh W. and Steele, W Glenn Jr., 1989, “Experimentation and Uncertainty Analysis for Engineers.” John Wiley and Sons, pp 89-100, 172-174

***Appendix A –
Flow loop schematic with pertinent instrumentation included***

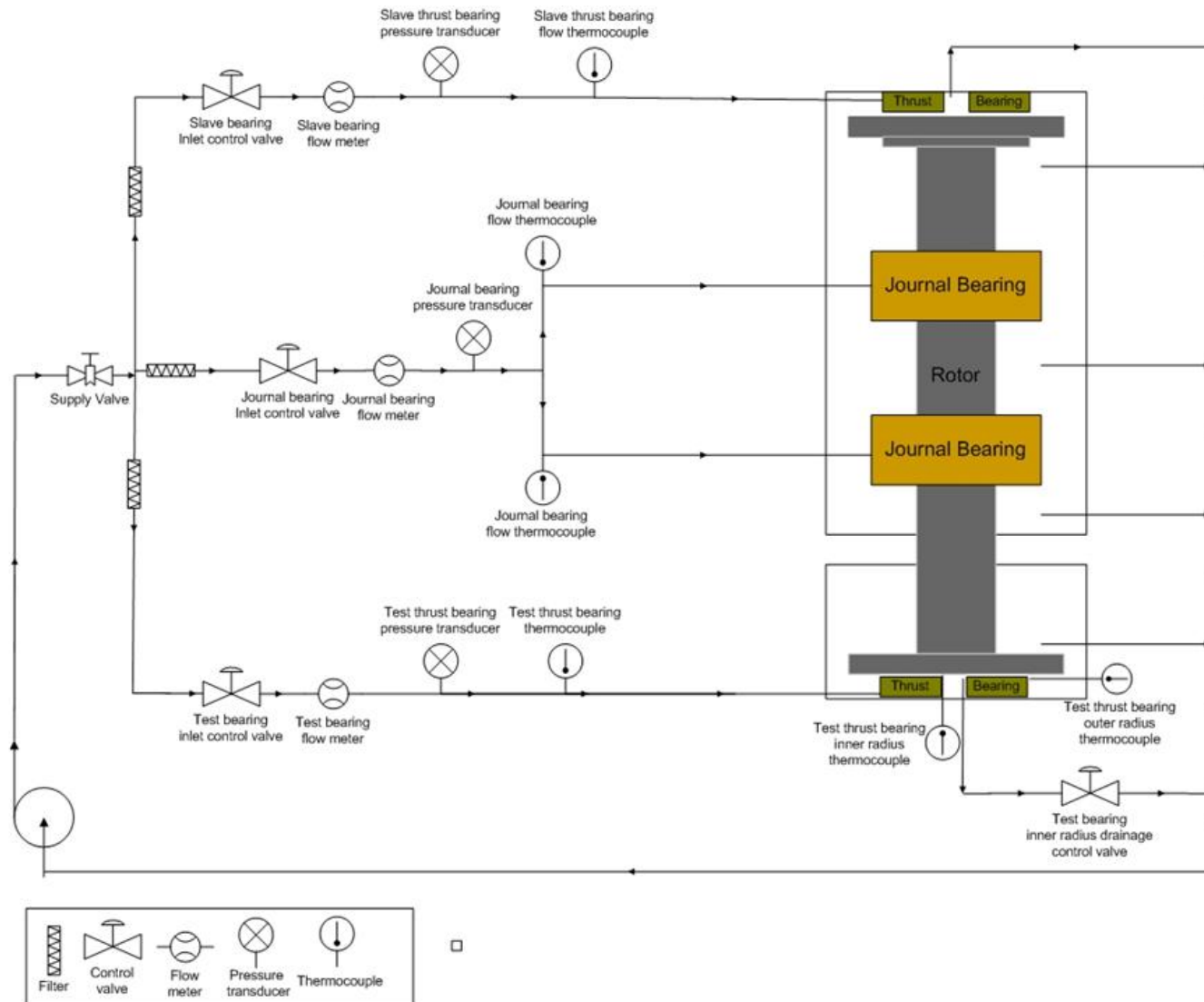


Figure 32: Hybrid thrust bearing test rig flow loop with select instrumentation locations included

***Appendix B –
Table of instrumentation and accessories used***

Item description		Manufacturer's part number		Desired range	Sensor range	Power requirements	Output	Resolution
Vendor - SKF								
Drivers	CMSS 65 5mm Probe	CMSS 66-002-00-12-10	Test thrust bearing probe system driver	1-20 mil	10-90 mil	-24V at 15mA	0 to -18V	200 mV/mil
	CMSS 65 5mm Probe	CMSS 66-002-00-26-10	Radial probe system driver	6 mil	10-90 mil	-24V at 15mA	0 to -18V	201 mV/mil
Proximity Probes	CMSS 65 sensor	CMSS 665	Sensors for the drivers					
Extension Cables	4 meter extension cable		Extension cables for proximity probe system					
Vendor - FTI								
	FT-10	FT-10NEXW-LEG-2	Radial bearing inlet flow meter	8-15 GPM	0.3-15 GPM			
	FT8-8	FT8-8NEXW-LEG-2	Test bearing inner radius discharge flow meter	0-4.75 GPM	0.16-7.5 GPM			
	FT-12	FT-12NEXW-LEG-2	Test bearing inlet flow meter	0.27-13.45 GPM	0.25-20 GPM			
Digital Indicator	FTI Linear Link	BR30-2-C-4	Linearizes and outputs flowmeter reading ****All Flowmeters require one			24V at 300mW	4-20 mA	±0.1% of reading
Vendor - Omega								
Pressure Transducer	Omega PX209 Pressure Transducer	PX209-300G5V	Test thrust bearing lands/pocket pressure transducers	0-250psi	0-300 psi	24V at 15mA		0.75 psi
	Omega PX209 Pressure Transducer	PX209-300G5V	Test thrust bearing inlet pressure transducer	0-250psi	0-300 psi	24V at 15mA		0.75 psi
	Omega PX209 Pressure Transducer	PX209-300G5V	Journal bearing inlet pressure transducer	0-250psi	0-300 psi	24V at 15mA		0.75 psi
Transducer Displays	Signal display and output	DP25B-E-A	Displays for pressure transducers			120Vac	± 5V	0.02% of reading
	Signal display and output (Thermocouples)	DP25B-TC-A	Displays for thermocouples			120Vac	± 5V	0.5° C
Thermocouple wire	100 ft, Polyvinyl, 24 AWG, Type K	PR-K-24-100	Wire for thermocouples on outer and inner test thrust bearing radius					
Vendor - ENCORE								
Amplifier	Proximity sensor amplifier	Encore Model 619M-002				-24V to 24V		
Rack w/ Power Supply	Rack and power supply for amplifiers	Encore Model 4015-124				120Vac	-24V to 24V	

***Appendix C –
Test thrust bearing rotor thrust disk plane equation derivation***

Determining the position and orientation of the thrust disk relative to the test thrust bearing is critical. The output of three eddy current probes is available for this task. The layout geometry of the probes is known as seen in Figure 33.

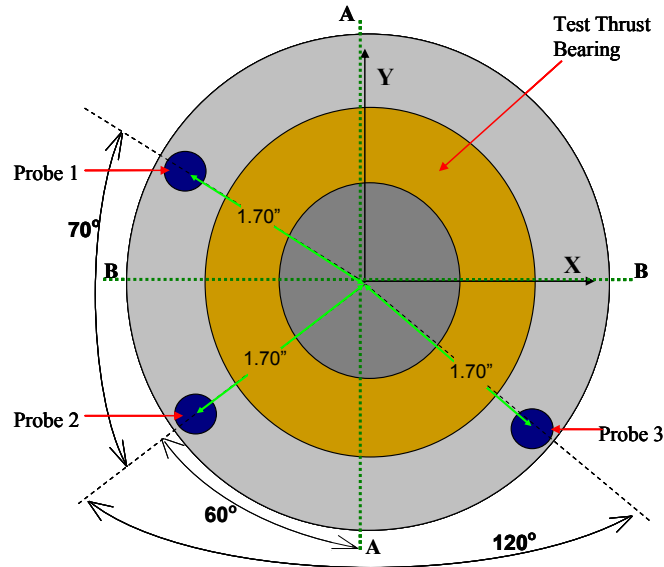


Figure 33: Layout geometry of eddy current sensors on test thrust bearing support

From this diagram, the horizontal and vertical positions of each probe relative to the center of the bearing are calculated. These positions are shown in Table 4.

Table 4: Vertical and horizontal positions of proximity probes on thrust bearing support from bearing center

	X	Y
Probe 1	-33.02 mm (-1.30 in)	27.69 mm (1.09 in)
Probe 2	-37.34 mm (-1.47 in)	-21.59 mm (-0.85 in)
Probe 3	37.34 mm (1.47 in)	-21.59 mm (-0.85 in)

The equation for the plane of the rotor thrust disk relative to the thrust bearing face can now be found. Both the thrust bearing face and the rotor thrust disk are assumed to be rigid flat planes. The three proximity probe outputs are used to identify three points on the plane of the thrust disk as shown in Figure 34.

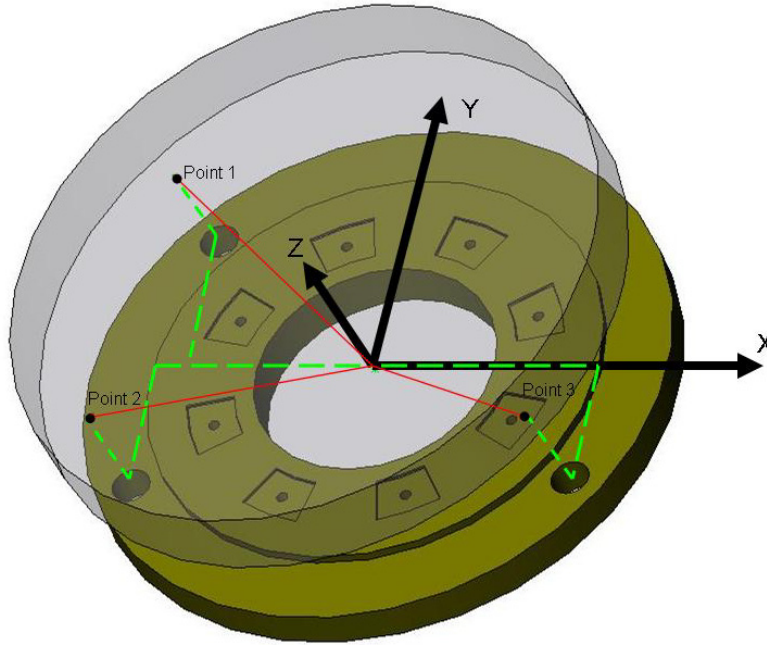


Figure 34: Depiction of the three points measured with the proximity probes on the test thrust bearing thrust disk face.

These three points on the thrust disk are further defined in Table 5.

Table 5: Coordinates of the three proximity probe points

	Point Coordinates (x,y,z)
Point 1	$(-33.02, 27.69, Z_1)$ mm $(-1.30, 1.09, Z_1)$ in
Point 2	$(-37.34, -21.59, Z_2)$ mm $(-1.47, -0.85, Z_2)$ in
Point 3	$(37.34, -21.59, Z_3)$ mm $(1.47, -0.85, Z_3)$ in

These three points can next be used to generate two vectors located on the surface of the plane. Equation (2.1) and (2.2) show these two vectors.

$$\vec{v}_{12} = \text{Point 2} - \text{Point 1} = \langle -4.32, -49.28, Z_2 - Z_1 \rangle \text{ mm} \quad (2.1)$$

$$\vec{v}_{13} = \text{Point 3} - \text{Point 1} = \langle 70.36, -49.28, Z_3 - Z_1 \rangle \text{ mm} \quad (2.2)$$

Where

\vec{V}_{12} = Vector from point 1 to point 2 in the thrust disk plane

\vec{V}_{13} = Vector from point 1 to point 3 in the thrust disk plane

Z_1, Z_2, Z_3 = Z coordinate of probe 1, 2, or 3

The two generated vectors can next be used to create a vector normal to the plane by taking the cross product of the two vectors.

$$\begin{aligned} \vec{N} &= \vec{V}_{12} \times \vec{V}_{13} \\ \vec{N} &= \langle 49.28(Z_2 - Z_3), -74.68Z_1 + 70.36Z_2 + 4.32Z_3, 144.87 \rangle \text{ mm} \end{aligned} \quad (2.3)$$

Where

\vec{N} = Normal vector to the thrust disk plane

A generic vector must now be generated from the first point and a generic point located on the plane of the thrust disk (x,y,z). Equation (2.4) shows the formula for this point.

$$\vec{V}_{\text{generic}} = \text{Generic Point} - \text{Point 1} = \langle x+33.02, y-27.69, z-Z_1 \rangle \text{ mm} \quad (2.4)$$

Where

\vec{V}_{generic} = Vector from point 1 to a generic point (x,y,z) in the thrust disk plane

Finally, by taking the dot product of the normal vector and the generic vector the equation of the thrust disk plane can be determined.

$$\begin{aligned} \vec{N} \cdot \vec{V}_{\text{generic}} &= 0 \\ 49.3(Z_2 - Z_3)x + (-74.7Z_1 + 70.4Z_2 + 4.3Z_1)y + 144.8z + (-63.5Z_1 - 12.7Z_2 - 68.8Z_3) &= 0 \end{aligned} \quad (2.5)$$

This equation can ultimately be reduced to the more useful, final form.

$$\begin{aligned} Z(x, y) &= M_1x + M_2y + Z_c \\ Z(x, y) &= 8.6(Z_3 - Z_2)x + (13.1Z_1 - 12.3Z_2 - 0.76Z_3)y + (11.1Z_1 + 2.2Z_2 + 12.1Z_3) \end{aligned} \quad (2.6)$$

Where

M_1 = Slope of the thrust disk plane in the X-axis

M_2 = Slope of the thrust disk plane in the Y-axis

Z_c = Clearance at the center of the test thrust bearing

***Appendix D –
Detailed figures of misalignment across bearing face and pocket
pressures***

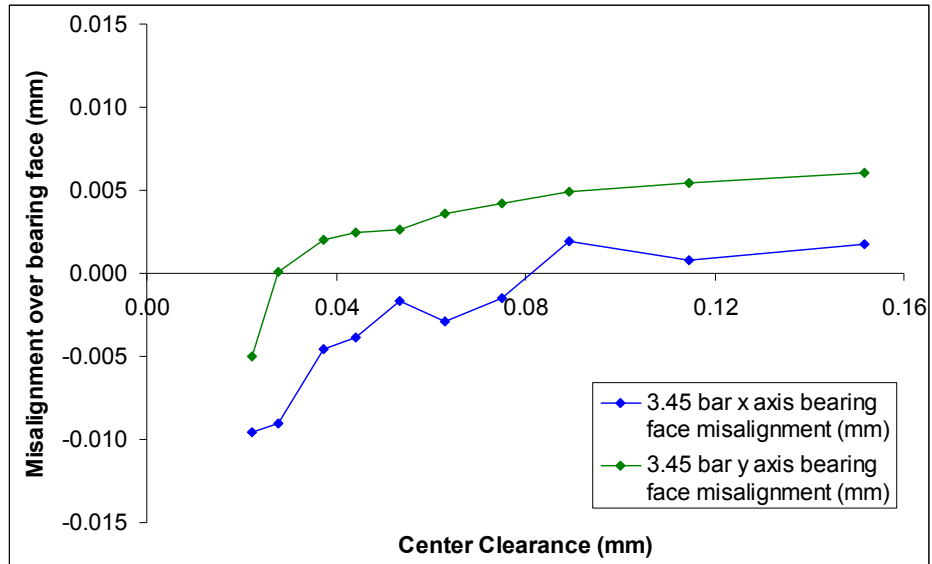


Figure 35: Misalignment over the bearing face about the x and y axis for 3.45 bar test thrust bearing supply pressure.

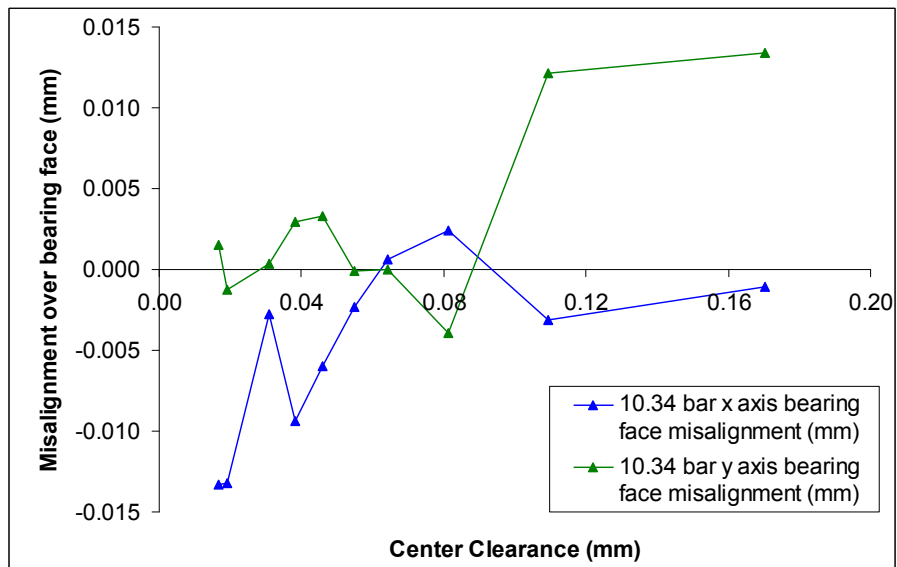


Figure 36: Misalignment over the bearing face about the x and y axis for 10.34 bar test thrust bearing supply pressure.

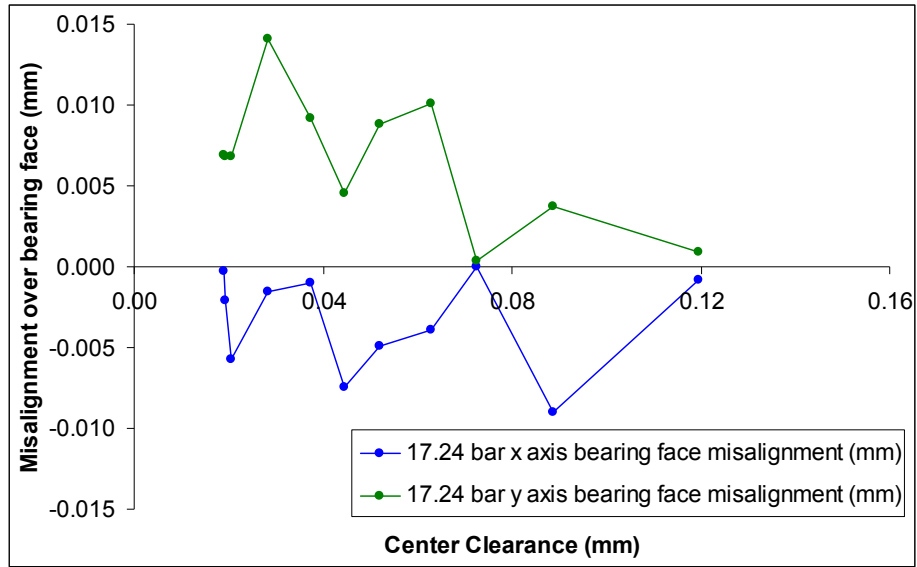


Figure 37: Misalignment over the bearing face about the x and y axis for 17.24 bar test thrust bearing supply pressure.

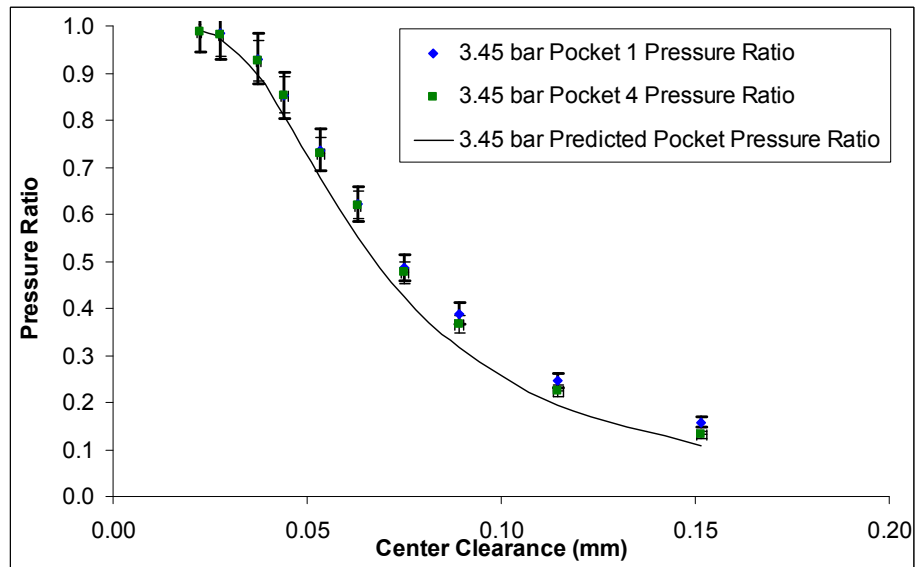


Figure 38: Pocket pressure ratios over the tested clearance range for 3.45 bar thrust bearing supply pressure.

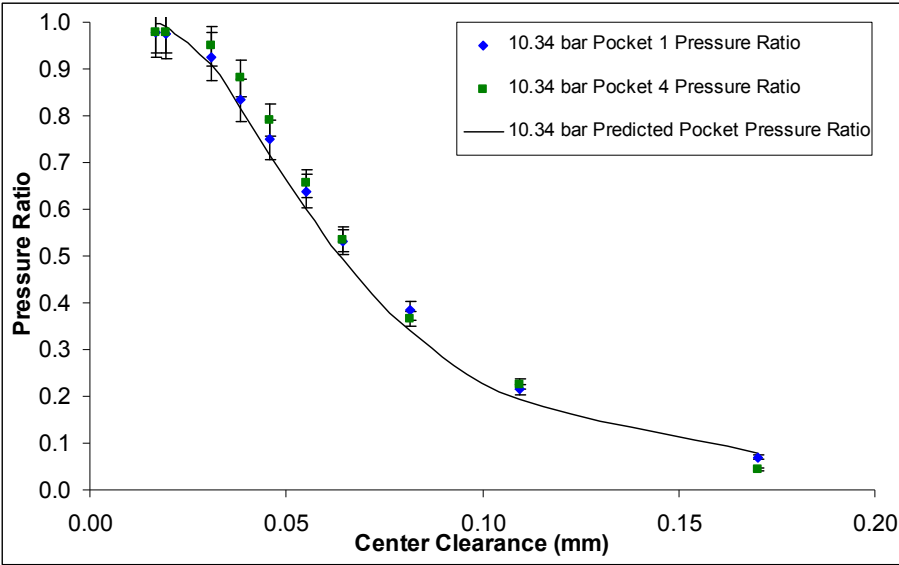


Figure 39: Pocket pressure ratios over the tested clearance range for 10.34 bar thrust bearing supply pressure.

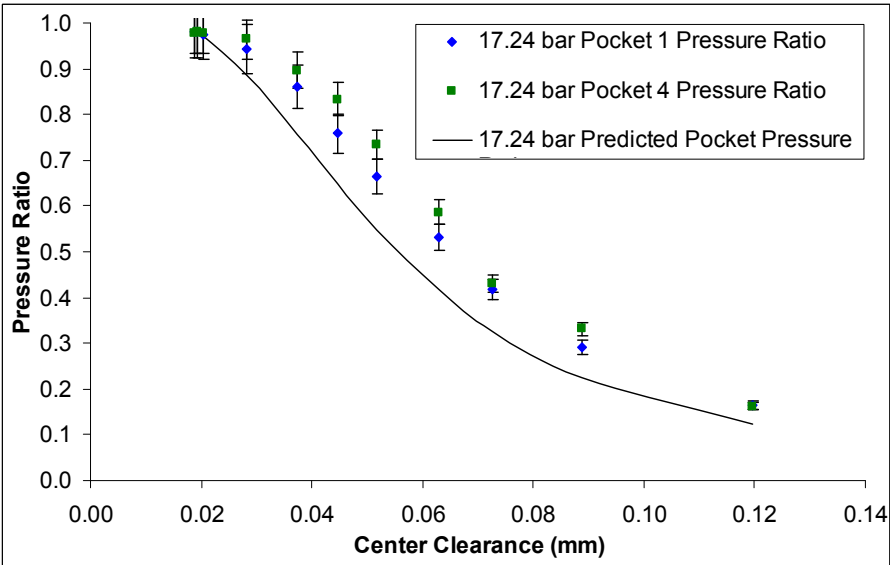


Figure 40: Pocket pressure ratios over the tested clearance range for 17.24 bar thrust bearing supply pressure.

***Appendix E –
Uncertainty analysis of experimental measurements***

To determine the validity of any experimentally obtained data sets, the error must be estimated. Errors can come from two sources (bias and precision). In this analysis, bias error is considered negligible and precision error is assumed to be the major error source. The precision error can come from several sources and must be propagated appropriately. To combine these errors Equation (3.1) [1] is used.

$$E_N = \left[\sum \left(\frac{dF(X_1, X_2, \dots, X_N)}{dX_N} * E_{XN} \right)^2 \right]^{1/2} \quad (3.1)$$

With this equation, so long as the function and individual variable errors are known, the overall error can be estimated. The measurement uncertainty (σ) can also be included into Equation (3.1) as one half of a summed squared term. Most of these individual errors are known from the error of the instrumentation; however, to determine the error from the calibration of the instrumentation Equation (3.2) [1] must be introduced,

$$SEE = \left[\frac{\sum [Y_i - (aX_i - b)]^2}{M - 2} \right]^{1/2} \quad (3.2)$$

to determine the standard error of estimation (SEE). The SEE can then be used similarly to determine standard deviation of the error associated with a given curve fit parameter. The error derived from the SEE that is associated with a given variable is $2*SEE$. This error band to either side of the calculated value will include approximately 95% of the possible points. With these two equations the errors of the experimental measurements are defined.

Equation (3.3) was used to define the flow rate.

$$FlowRate = A_{FlowMeter} * V - B_{FlowMeter} \quad (3.3)$$

Where

$A_{FlowMeter}$ = Linear calibration constant of the flow meter

$B_{FlowMeter}$ = Flow meter calibration offset

V = Flow meter output voltage

This equation can then be used with Equation (3.1) to find the expression for overall error.

$$E_{Flowrate} = \sqrt{(V * E_{AFlowMeter})^2 + (A_{FlowMeter} * E_V)^2 + (2 * \sigma_{Flow})^2} \quad (3.4)$$

Where

$E_{FlowMeter}$ = Flow meter error

$E_{AFlowMeter}$ = Error of $A_{FlowMeter}$ term

E_V = Error of flow meter voltage measurement

σ_{Flow} = Standard deviation of flow meter reading

This process can be repeated to find the error associated with the load measurement from

$$Load = A_{LoadCell} * V - B_{LoadCell} \quad (3.5)$$

Where

$A_{LoadCell}$ = Linear calibration constant of the load cell

$B_{LoadCell}$ = Load cell calibration offset

V = Load cell output voltage

Applying Equation (3.1) to Equation (3.5) the error expression is

$$E_{Load} = \sqrt{(A_{Load} * E_V)^2 + (2 * \sigma_{Load})^2} \quad (3.6)$$

Where

E_{Load} = Load cell error

E_V = Error of load cell voltage measurement

σ_{Load} = Standard deviation of flow meter reading

Finally the error associated with the differentiation estimation of the stiffness can be determined using

$$E_{dF/dZ} = \sqrt{E_A^2 + E_B^2 + E_C^2 + E_D^2} \quad (3.7)$$

Where

$$Load = A * Z_C^4 + B * Z_C^3 + C * Z_C^2 + D * Z_C + E$$

E_N = Error associated with term N

Z_C = Thrust bearing clearance

This equation requires that the error from each term is known; hence, the TableCurve2D software was utilized. This software calculated the error from each of the terms in the polynomial curve fit load expression. These errors were then substituted into Equation (3.7).